

DESIGN METHODOLOGY OF A FAST
CHARGING BATTERY MODULE

DESIGN METHODOLOGY AND MODELLING OF A FAST
CHARGING BATTERY MODULE AND THERMAL
MANAGEMENT SYSTEM FOR ELECTRIC VEHICLES

BY

JEREMY MICHAEL LEMPert, B.Eng.Management

A THESIS

SUBMITTED TO THE DEPARTMENT OF MECHANICAL ENGINEERING

AND THE SCHOOL OF GRADUATE STUDIES

OF MCMASTER UNIVERSITY

IN PARTIAL FULFILMENT OF THE REQUIREMENTS

FOR THE DEGREE OF

MASTER OF APPLIED SCIENCE

© Copyright by Jeremy Michael LEMPert, August 2020

All Rights Reserved

Master of Applied Science (2020)
(Mechanical Engineering)

McMaster University
Hamilton, Ontario, Canada

TITLE: Design Methodology and Modelling of a Fast Charging
Battery Module and Thermal Management System for
Electric Vehicles

AUTHOR: Jeremy Michael LEMPert
B.Eng. Management (Mechanical Engineering and Man-
agement)
McMaster University, Ontario, Canada

SUPERVISORS: Dr. Ali EMADI and Dr. James COTTON

NUMBER OF PAGES: xx, 117

To my family, for your endless love and support.

Lay Abstract

As electric vehicles gain traction in the market, long charging times remain a key sticking point. Significantly reduced charging times are possible, but require a thorough understanding of the battery cells and pack, as well as thoughtful selection of components and system design. Effective temperature control is required to remove heat generated within cells and ensure safe operation and proper lifespan of the battery pack.

This thesis presents a methodology for the development of a battery module for fast charging, including selection of a suitable battery cell and design of a thermal management system. Four different cells are compared based on experimental testing and a cell is selected for use in a prototype module. Models of the module are developed using physics- and machine learning-based approaches. The prototype module is tested in a laboratory for a series of fast charges, and temperature measurements are compared to model predictions.

Abstract

With electric vehicles (EVs) emerging as a means to reduce transportation-related greenhouse gas emissions, battery charging times and range anxiety remain a key sticking point. While the electrochemical batteries that power EVs cannot compete with liquid fuels on the basis of energy density, higher efficiencies and large battery packs make it possible to achieve competitive driving range. Reduced charging times, however, remain a challenge spanning many disciplines, where cell selection and thermal management play a critical role

For the development of a fast charging, liquid-cooled battery module, the research outlined in this thesis presents a design methodology including the processes of selection and characterization of a suitable battery cell, modelling of heat generation inside the cells, and design and modelling of a thermal management system.

Four different cells are compared. The cells are first characterized in a laboratory, and suitability for fast charging is evaluated based on the experimental results. Simplified thermal models are used for comparison of the cells. Factors such as charging efficiency and required cooling system size are considered. A three-cell, liquid-cooled

test module is designed and constructed for a selected cell, and further characterization is conducted in order to develop a detailed loss model.

Thermal modelling is accomplished using numerical models, developed using knowledge and assumptions of the underlying physics and material properties, and using a neural network-based approach—which can be developed without such knowledge or assumptions, but requires data from laboratory testing of the cell, module, or pack of specific interest. Results from the numerical model and neural network-based model are compared to experimental data at charge rates up to 5C and for a cycle of repeated driving with periodic fast charging. For a 5C charge, a peak temperature of 34.6 °C is measured in the laboratory, and modelled to within 0.6 °C.

Acknowledgements

I would like to thank all of my classmates and fellow students, and the staff and faculty at McMaster who kept a smile on my face, and made it feel so incredibly warm through the last seven years. To my second family at the McMaster Automotive Resource Center and Department of Mechanical Engineering, thank you for the collaboration and the excellent company, and for the opportunity to learn so much from so many of you. Thank you to all the friends who I made along the way, who were there when I needed help and who I enjoyed spending my time with.

Thank you to my supervisors, Dr. Ali Emadi and Dr. James Cotton, for your mentoring and for giving me the opportunity to grow as a graduate student. To you both, and also to Dr. Saeid Habibi and Cam Fisher, thank you for the test facilities that made this work possible.

To Dr. Phillip Kollmeyer, thank you for your guidance and mentoring throughout my master's career, and for your contributions and involvement in all the work that makes up this thesis. To Melissa He and Mike Hausman, thank you for the design and fabrication of the battery module used in this thesis, and for your contributions to work contained in this thesis, including the cell selection and comparative modelling.

Thank you to Brendan Sullivan and Andrew George for your collaboration on the neural network implementation, to Carlos Vidal for your guidance in designing the neural networks, and to Romina Rodriguez and Luis Lopera for your valuable advice on the numerical modelling.

Thank you to the Westdale Wastrels Cycling Club for keeping me in shape, out of trouble, and excited to get up at 5:00am to face 5 °C headwinds with little to no layering—and for the post-ride coffees, endless banter, and play-by-play recaps to start my days.

And thank you to Iman Aghabali and Mehdi Eshaghian, for your incredible thoughtfulness and senses of humour, and for bringing energy to every room you entered. I will carry your memories with me forever.

Abbreviations

AC	Alternating Current
CC-CV	Constant-Current, Constant-Voltage
CFD	Computational Fluid Dynamics
ECM	Equivalent Circuit Model
EV	Electric Vehicle
HPPC	Hybrid Pulse Power Characterization
ICE	Internal Combustion Engine
LFP	Lithium Iron Phosphate
Li-ion	Lithium-Ion
LSTM	Long Short-Term Memory
LUT	Lookup Table
NCA	Lithium Nickel Cobalt Aluminum Oxide

NMC	Lithium Nickel Manganese Cobalt Oxide
NN	Neural Network
OCV	Open-Circuit Voltage
RMSE	Root-Mean-Square-Error
RNN	Recurrent Neural Network
SEI	Solid Electrolyte Interface
SOC	State of Charge

Statement of Co-Authorship

The material contained in Chapter 5 is adapted from publicized work involving co-authors. The majority of the contributions to the paper are based on work by the first author. The following describes the contributions of each author and describes the contributions of Jeremy M. Lempert, the author of this thesis:

Lempert, J., Kollmeyer, P., Malysz, P., Gross, O., Cotton, J., Emadi, A., "Battery Entropic Heating Coefficient Testing and Use in Cell-Level Loss Modeling for Extreme Fast Charging," SAE International Journal of Advances and Current Practices in Mobility 2020-01-0862, 2020, <https://doi.org/10.4271/2020-01-0862>.

In this journal paper, J. Lempert was responsible for the literature review, design and execution of the test plan, analysis of results, modelling, and written manuscript. Dr. P. Kollmeyer contributed to the development of the battery module and experimental apparatus, including data collection. Dr. P. Kollmeyer, Dr. P. Malysz, O. Gross, Dr. J. Cotton, and Dr. A. Emadi contributed to the layout of the paper, discussion of the results, revisions, and proofreading.

Contents

Lay Abstract	iv
Abstract	v
Acknowledgements	vii
Abbreviations	ix
Statement of Co-Authorship	xi
1 Introduction	1
1.1 Motivation	3
1.2 Contributions	4
1.3 Thesis Outline	4
2 The Road to Fast Charging in Electric Vehicles	7
2.1 Background and Challenges	7
2.1.1 Energy and Power Density	8
2.1.2 Safety	10

2.1.3	Cell Ageing	11
2.1.4	Thermal Management	14
2.2	Fast Charging Infrastructure	15
2.3	Prior Art	16
2.3.1	Battery Cell Loss Modelling	16
2.3.2	Battery Thermal Modelling	18
2.3.3	Battery Thermal Management Solutions	21
2.3.4	Fast Charging Implementation	23
3	Cell Testing and Selection for Fast Charging	25
3.1	Specifications of Cells Tested	26
3.2	Equipment and Experimental Setup	27
3.3	Cell Characterization	28
3.3.1	Measured Cell Data for a Range of Fast Charge Rates	29
3.3.2	Cell Performance as a Function of Charge Rate	30
3.3.3	Pack Performance as a Function of Charge Rate	32
3.4	Required Cooling System Size Comparison	33
3.4.1	Thermal Model Properties and Boundary Conditions	35
3.4.2	Thermal Modelling Results	36
3.4.3	Double-sided versus Single-sided Cooling	37
3.4.4	Comparison of Cell and Cooling System Options	39
4	Experimental Inter-cell Cooling Module	42
4.1	Geometry and Design	42

4.2	Component Specifications	44
4.3	Instrumentation	47
5	Loss Modelling with Entropic Heating Coefficient	49
5.1	Battery Cell Loss Model	50
5.2	Entropic Heating Coefficient Measurement	51
5.2.1	Development of a Test Program	53
5.2.2	Compensation for Self-Discharge and Voltage Relaxation	56
5.3	Behavior of the Entropic Heating Coefficient	59
5.4	Entropic Heating Coefficient Map	60
5.5	Loss Modelling with Entropic Heating Coefficient	63
5.5.1	Reversible Heating Contribution	65
5.5.2	Temperature Contribution	66
5.5.3	Peak Loss Comparison	67
6	Module Thermal Modelling	69
6.1	CFD-based	70
6.1.1	Detailed Steady State Thermal-Fluid Model	71
6.1.2	Thermal-Only Transient Model	74
6.2	Neural Network-Based	76
6.2.1	Architecture and Training	77
7	Module Experimental Measurements and Validation of Thermal Modelling	81
7.1	Steady State	84

7.1.1	Measured and CFD-Modelled Temperature for Constant Loss	84
7.2	Transient	86
7.2.1	CFD-Based	86
7.2.2	Neural Network-Based	91
7.2.3	Comparison of Modelling Methods	99
8	Conclusion	101
8.1	Future Work	104
	References	106

List of Tables

3.1	Battery cell specifications.	26
3.2	Battery cell cycler specifications.	27
3.3	Environmental chamber specifications.	28
3.4	Charge protocol for cells over charge-rate range.	29
3.5	Simplified thermal model properties.	35
3.6	Selected plate thickness, p , and comparison of selected cell and cooling system options.	40
4.1	Thermal properties of the materials used in the test module.	43
4.2	Dimensions of test module components.	44
4.3	Properties of ethylene glycol-water solution.	44
5.1	Test points for entropic heating coefficient test grid.	54
6.1	Mesh sensitivity study for coolant flow model.	73
6.2	Mesh sensitivity study for transient thermal model.	75
7.1	Temperature prediction error at steady state.	85
7.2	Validation RMSE of the different networks.	98

List of Figures

2.1	Ragone plot for EV applications.	9
2.2	Li-ion cell temperature and voltage operating window.	10
2.3	Thermal runaway chain reaction in fast charged cells.	11
2.4	Arrhenius plot showing Li-ion cell ageing caused by cycling at 1C. . .	12
2.5	Modelled impact of cell temperature on cycle life at various charge rates and for cells of different energy density.	13
2.6	Li-ion cell form factors.	15
2.7	Pouch cell cold plate.	22
2.8	“Wavy profile” cooling tube used in Tesla battery packs.	23
3.1	Battery cells tested.	27
3.2	Measured fast charge data for each cell type.	30
3.3	Fast charge performance as a function of charge rate.	31
3.4	Comparison of fast charging time and pack loss.	33
3.5	Simplified, three-dimensional thermal model, before applying symmetry planes.	34

3.6	Predicted temperature rise versus cooling method and inter-cell cooling plate thickness p for a 4C charge rate case.	36
3.7	Temperature <i>rise</i> for 4C charge versus cooling plate placement for A123 NMC cell with $p = 0.5$ plate thickness.	38
3.8	Temperature <i>rise</i> for 4C charge versus cooling plate thickness and placement for A123 NMC cell.	39
4.1	Prototype 3p1s battery module with $p = 0.26$ cooling plates, and placement in environmental chamber	46
4.2	Prototype 3p1s battery module with embedded thermocouples.	48
5.1	Circuit diagram of test setup.	53
5.2	Environmental chamber temperature program for each SOC point.	55
5.3	OCV vs. Time before and after applying the correction for self-discharge rate.	57
5.4	Correction factors derived from rate of change of OCV with time ($\partial OCV/\partial t$) at thermal equilibrium.	58
5.5	Corrected OCV response yielding positive entropic heating coefficient.	59
5.6	Corrected OCV response yielding negative entropic heating coefficient.	60
5.7	Entropic heating coefficient map obtained from testing.	61
5.8	Entropic heating coefficient map without compensation for self-discharge and voltage relaxation.	62
5.9	Modelled cell losses for a 1C charge.	64
5.10	Modelled cell losses for a 3C charge.	64
5.11	Modelled cell losses for a 5C charge.	65

5.12	Maximum and minimum reversible heat generation rate as a percentage of maximum irreversible heat generation rate.	66
5.13	Peak cell loss for a series of 4C charges at different temperatures. . .	67
5.14	Peak cell loss shown for a series of 20 °C charges from 1C to 5C. . . .	68
6.1	Geometry of thermal-fluid model.	72
6.2	Mesh of detailed, steady state thermal-fluid model.	74
6.3	Geometry of thermal-only model.	75
6.4	Mesh of thermal-only model.	76
6.5	Architecture of the recurrent neural networks	78
6.6	MATLAB Training Progress window, showing training of interpolative network.	79
7.1	Cell and module temperature measurements for a 5C charge.	82
7.2	Measured cell face temperature and current magnitude for a 5C charge.	83
7.3	Measured cell face temperature and current magnitude for a 3C charge.	84
7.4	Measured peak cell surface temperature for a series of charge rates. .	86
7.5	Measured and modelled cell face temperature for varying cell specific heat.	88
7.6	Battery module current and SOC for repeated US06 drive cycles and 4C fast charges.	90
7.7	Measured and modelled temperatures for repeated US06 drive cycles and 4C fast charges.	90
7.8	Interpolative network predicted maximum cell temperature compared to measured values for 2C and 4C charges (validation set).	91

7.9	Interpolative network predicted maximum cell temperature <i>difference</i> compared to measured values for 2C and 4C charges (validation set).	92
7.10	Bilateral extrapolation network predicted maximum cell temperature compared to measured values for 1C and 5C charges (validation set).	93
7.11	Bilateral extrapolation network predicted maximum cell temperature <i>difference</i> compared to measured values for 1C and 5C charges (validation set).	94
7.12	Unilateral extrapolation network predicted maximum cell temperature compared to measured values for 4C and 5C charges (validation set).	95
7.13	Unilateral extrapolation network predicted maximum cell temperature <i>difference</i> compared to measured values for 4C and 5C charges (validation set).	95
7.14	Percentage error of predicted maximum cell temperature <i>difference</i> as compared to experimental data (for respective validation sets).	97
7.15	Measured and modelled cell surface temperature for 2C and 4C charges.	99

Chapter 1

Introduction

Amid growing concerns over climate change and environmental degradation, electric vehicles (EVs) have emerged as an alternative to conventional, internal combustion engine (ICE) vehicles. Electric vehicles utilize energy stored in electrochemical battery cells —typically lithium-ion (Li-ion)—which form a battery pack, while ICE vehicles source energy from on-board fossil fuels [1]. To date, Li-ion cells are preferred for these battery packs due to their combination of energy density, power density, and cycle life [2, 3].

Battery cells are arranged to form a battery pack, which may have an energy density two orders of magnitude less than that of gasoline [4, 5]. Despite this much lower energy density, EVs are able to achieve a driving range competitive with ICE vehicles due in part to their far higher conversion efficiencies; the tank-to-wheel efficiency of an EV is around 90% [5], approximately three times higher than that of an ICE-driven vehicle [6]. One of the main remaining shortfalls of EVs, however, is the

comparatively long time required to “fill the tank”—i.e. recharge the battery—which is often cited as a significant factor hindering their wider adoption [7]. Charging the battery of an EV may take more than eight hours using a Level 2 charger, which draws power from a single-phase outlet, typically at around 6 kW—while the full driving range of an ICE vehicle can be restored in just a few minutes by filling the tank at a roadside fuel station. Fast charging aims to address this gap, with charging rates of 350 kW [8] and beyond. Since fast charging functionality is correlated with reduced range anxiety amongst consumers, it is expected to expedite the adoption of EVs.

For a fast-charging-capable Li-ion battery module, this thesis explores cell characterization, cell selection, thermal management system design, and modelling of heat generation and thermal response during fast charging and over the course of a drive cycle. Test cells are first characterized in a laboratory in order to determine their open-circuit voltage (OCV), internal resistance, and pulse power capabilities, each as a function of state of charge (SOC). The cells are then charged at increasing rates up to 5C and 10C. Using cell loss data recorded in the laboratory, simplified thermal models are constructed to compare each cell’s performance for different cooling plate configurations. An effective module energy density for each cell is determined by considering the mass of cooling system components—adding consideration for cooling requirements of each cell and facilitating a more effective comparison of cells. For a selected battery cell and cooling system configuration, a liquid-cooled, experimental test module is constructed. Models are developed for estimation of internal

heat generation and thermal response of the module, conducted using two different approaches: computational fluid dynamics (CFD) and recurrent neural networks (RNNs). For a series of fast charges and a combined drive cycle and fast charge profile, temperatures obtained from the thermal models are compared to those obtained from laboratory measurements of the module.

1.1 Motivation

There is a significant amount of interest in decreased charging times for the next generation of EVs. With higher charge rates, however, it becomes essential to carefully monitor and control the temperature of the battery pack to avoid accelerated ageing and thermal runaway of the cells, which may lead to catastrophic failure of the battery pack.

Fast charging presents many new challenges. As it leads to very high rates of heat generation in battery cells, care must be taken to maintain the cell temperature to within an acceptable range, and the temperature uniformity to within an acceptable limit. Failure to effectively manage temperatures may lead to accelerated degradation of the cells and thermal runaway [2, 9, 10].

Cell selection plays a central role. Characteristics such as energy density, cycle life, and over-potential resistance are important factors in determining the suitability of a specific cell for fast charging EV applications [11, 12]. Cell selection also determines the design of the battery pack, which then affects its effective energy density. A cell with high energy density and low power density will require a more intensive

cooling strategy, which then reduces the effective energy density of the battery pack.

Thermal models are used throughout the design phase for the development of charging protocols and thermal management systems. In production vehicles, simplified reduced-order models may be deployed online to augment temperature measurements and increase resolution of the measured temperature distribution while reducing the number of embedded sensors [13], thus reducing costs.

1.2 Contributions

This thesis presents a battery module design and modelling methodology, with a focus on thermal management to enable high-powered charging in electric vehicles. Novel contributions include cell characterization for, and deployment of, a battery cell heat generation model—a critical input for thermal modelling which has not yet seen much discussion and involves quantification and isolation of minute changes in open-circuit voltage with temperature. This heat generation model is then used in thermal modelling of a liquid-cooled battery module for charge rates up to 5C, and the results are validated against experimental data obtained for the module. Thermal modelling of battery cells and experimental validation at such high charge rates are not common in existing literature, and present unique challenges.

1.3 Thesis Outline

This thesis comprises eight chapters, this section presents an outline of the content.

In Chapter 1 (the present chapter), the research problem is defined and motivation

presented. Contributions to the state-of-the-art are discussed, and the structure of the thesis is outlined.

Chapter 2 explores the various challenges in implementing fast charging in electric vehicles, including safety and ageing considerations. This chapter also explores the prior art relevant to fast charging, with a focus on thermal modelling and management.

Chapter 3 explores the process of cell selection for fast charging applications. Cells are first characterized in a laboratory, then fast charging performance and thermal management system requirements are compared using simplified thermal models. From this, a cell is selected for use in the remaining chapters.

The experimental battery module is introduced in Chapter 4. Module geometry and cell configuration are discussed. The experimental data from this module are used in the remainder of the thesis in the cell and module characterization and for validation of the different models developed.

In Chapter 5, a model of battery cell loss is developed from an energy balance. The loss model requires characterization of the battery cells, including very delicate voltage measurements in response to cell temperature changes.

Chapter 6 details the modelling of the battery module during fast charging and over a drive cycle. Models are developed using commercial CFD software to predict temperatures throughout the module and flow characteristics of the cooling fluid. The CFD model utilizes the cell loss model developed in Chapter 5. A model is also developed utilizing neural networks for prediction of maximum temperature and maximum temperature difference across the surface of the cell in the module.

In Chapter 7, the results of the numerical thermal model and the neural network-based thermal model are compared to experimental temperature measurements. For the numerical model, temperatures are compared at steady state, during a series of fast charges, and during a combined, repeated drive cycle and fast charge profile. For the neural network-based model, results are compared to a series of fast charges, and the impact of training data selection is demonstrated.

Finally, Chapter 8 concludes the thesis, recalling the work performed and summarizing the findings. Recommendations for future work are also discussed in this chapter.

Chapter 2

The Road to Fast Charging in Electric Vehicles

While many technical challenges exist in the implementation of electric vehicle fast charging, many of these challenges continue to see extensive research interest. This chapter is not intended to be a comprehensive review across all research areas, but rather, aims to provide sufficient background and context for the content of this thesis.

2.1 Background and Challenges

Fast charging of EVs remains a challenge spanning many disciplines, including battery cell material selection and design, power delivery and conversion, controls, and thermal management.

2.1.1 Energy and Power Density

The energy density of the battery pack determines the *driving range* of the vehicle for a given mass (gravimetric) or volume (volumetric). The greater the amount of electrical energy that can be stored, the greater the driving range of the vehicle. The power density of the battery pack, on the other hand, determines the *performance* of the vehicle: acceleration, regenerative braking, and charging rates are all improved with increasing power density. Ideally, it would be feasible to independently maximize both the energy density and power density of a cell simultaneously. Unfortunately, however, these cell properties exist in mutual competition: energy density increases are often at the detriment of power density, and vice versa [7]. For example, cell electrode thickness may be increased in order increase energy density, however, this typically results in impeded mass transport within the cell, reducing the charge rate that can be achieved without sacrificing the life of the cell [14].

The Ragone plot is useful for visualizing energy and power densities of different energy storage options, and illustrates the trade-off between the two. A Ragone plot for EV applications is shown in Figure 2.1.

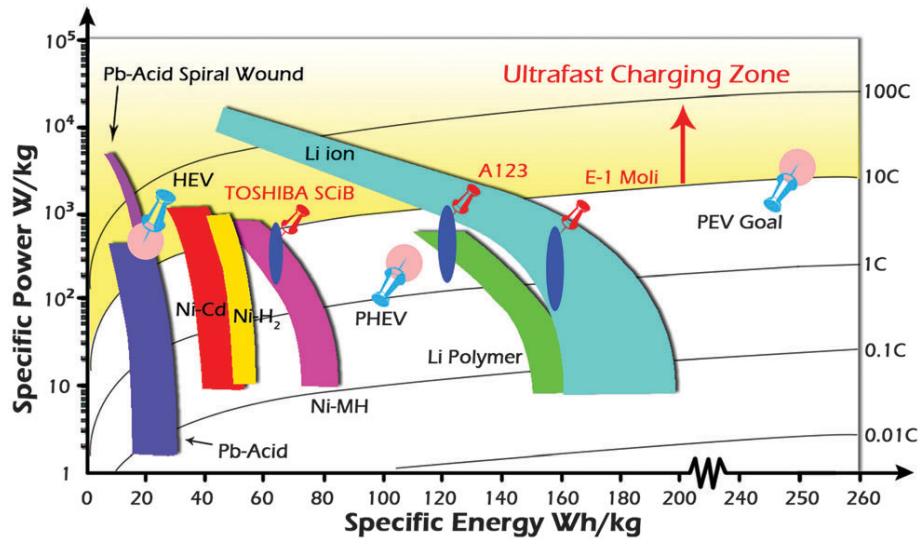


Figure 2.1: Ragone plot for EV applications, showing the performance of different energy storage solutions [15].

Figure 2.1 shows the typical range of performance possible from a Li-ion cell. The shortfall, as compared to the goal values for EVs, is indicated on this plot. For comparison, an automotive ICE is quoted at approximately 600 Wh kg^{-1} and 500 W kg^{-1} [16, 17], though it should be noted that the “charging” power density of an ICE would be far higher than this figure suggests, as this involves simply replenishing the fuel tank. The right-hand axis indicates the C-rate, which is defined as the instantaneous current applied divided by the total battery capacity. Thus, a rate of 1C represents the current required to discharge or charge a battery in one hour, while a rate of 2C represents the current required to do so in a half-hour.

2.1.2 Safety

Safe and sustainable operation of Li-ion cells is predicated on maintaining cell voltage and temperature within operational limits—this is especially challenging at high rates of charge and discharge. Exact limits depend on the active materials used, they are specific to each cell and are provided by the manufacturer. The typical operating window is shown in Figure 2.2.

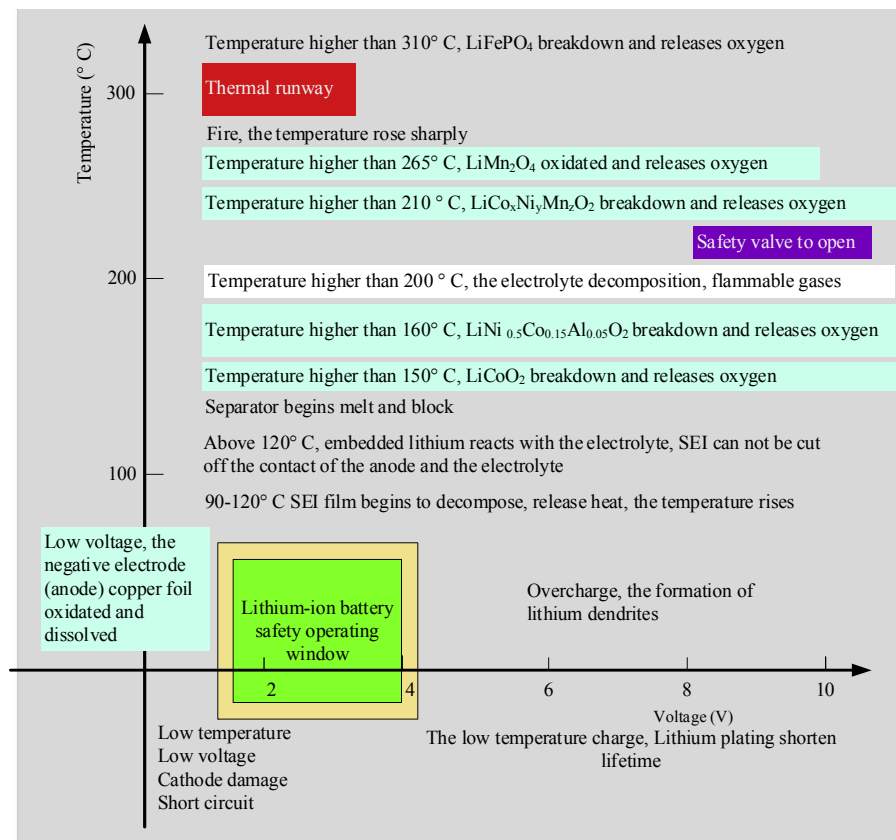


Figure 2.2: Li-ion cell temperature and voltage operating window [2, 18].

Figure 2.2 also shows the consequences of deviating from the operating window.

The greatest threat to safety is thermal runaway, which occurs when the cell temperature increases beyond a critical value and begins a series of chain reactions, ending in catastrophic failure. In the context of fast charging, thermal runaway often begins with a reaction between plated lithium and electrolyte. Thermal runaway process in fast charged cells is shown in Figure 2.3.

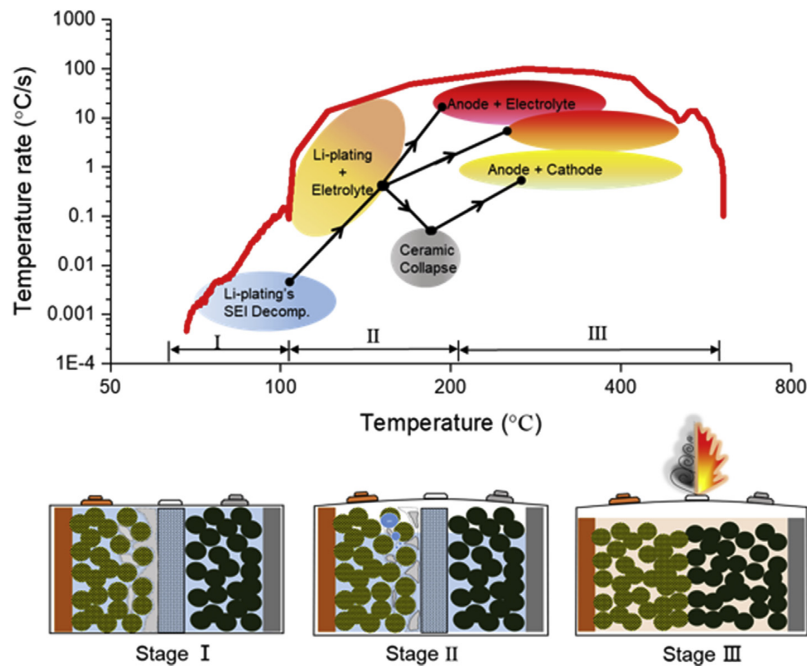


Figure 2.3: Thermal runaway chain reaction in fast charged cells [7, 19].

2.1.3 Cell Ageing

Even while operating Li-ion cells at *safe* temperatures, cell temperatures have severe implications on their *lifespan*. In a study of Li-ion cell ageing during cycling at a 1C-rate, at temperatures ranging from $-20\text{ }^{\circ}\text{C}$ to $70\text{ }^{\circ}\text{C}$, it is found that cycle life is maximized at a temperature of $25\text{ }^{\circ}\text{C}$ [20]. At temperatures below $25\text{ }^{\circ}\text{C}$, cell ageing is

found to be predominantly driven by lithium plating, which is increasingly prominent as temperature *decreases*. At temperatures above 25 °C, cell ageing is found to be predominantly driven by the growth of solid electrolyte interface (SEI) layers, which is increasingly prominent as temperature *increases*. This relationship is shown in the Arrhenius plot in Figure 2.4.

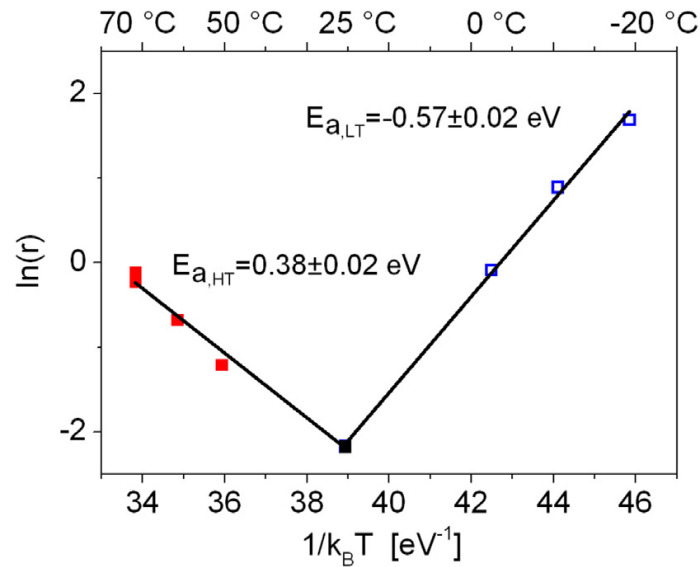


Figure 2.4: Arrhenius plot showing Li-ion cell ageing caused by cycling at 1C [20]. The natural logarithm of the ageing rate (r) is plotted against decreasing temperature (upper x -axis).

Furthermore, as C-rate and energy density increase (either independently or simultaneously), the cycle life-maximizing cell temperature is found to increase, since the risk of lithium plating becomes more pronounced at higher C-rates and for greater electrode thickness [12, 14]. Figure 2.5 shows the impact of charging rate on cell capacity loss for two modelled cells of different energy density. For fast charging applications, this shows that target cell temperature should be a function of desired

charging rate and the energy density of the cell, among other factors. *This also illustrates the importance of considering characteristics of the specific cell model when determining target cell temperatures for the thermal management system.*

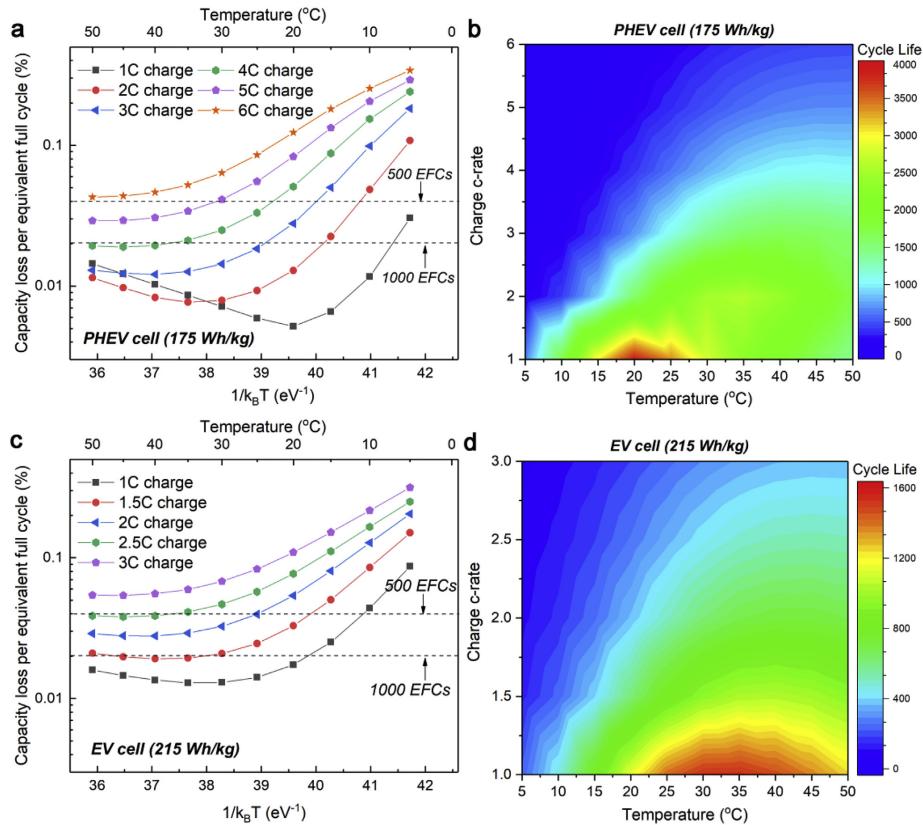


Figure 2.5: Modelled impact of cell temperature on cycle life at various charge rates and for cells of different energy density [12].

Maximizing cycle life of the electric vehicle battery is of utmost importance, as the battery pack is a significant contributor to the total cost of the vehicle [3]. While the study of physical mechanisms of cell ageing remain outside the scope of this thesis, the temperature and temperature gradients that contribute to ageing are central topics.

2.1.4 Thermal Management

From the Sections 2.1.2 and 2.1.3, it is clear that effective thermal management is critical in the battery packs of EVs. In addition to the safety and ageing considerations, cell temperature is known to have a significant impact on a charging efficiency, with internal resistance increasing significantly for decreasing temperature [21]. With charge rates reaching 350 kW and above, effective thermal management may lead to higher efficiency and tens of kilowatts of energy savings during charging [22]. Energy savings associated with increased charging efficiency are then compounded by reduced cooling loads. In implementing a thermal management system, care must be taken to avoid over-cooling the cells, as this would only lead to increased cooling loads and increased risk of lithium plating during fast charging, shortening the cycle life of the cells.

Pack layout and thermal management approach are dependent on the cell form factor, and selection of an appropriate cell form factor is a key step in the design of a battery pack. Li-ion cells are typically available in cylindrical, prismatic, or pouch form factors, as shown in Figure 2.6.

Smaller cells may offer greater flexibility in packaging and greater heat rejection capabilities, in addition to increased economies of scale and more mature technology. Cylindrical and prismatic cells with metallic casings also provide protection to the active materials against puncture and mechanical vibration [16]. A battery pack composed of large-format pouch cells, however, requires fewer cells, interconnectors, and control circuits, and may offer greater energy density. As the surface-to-volume ratio decreases, careful thermal management system design becomes increasingly

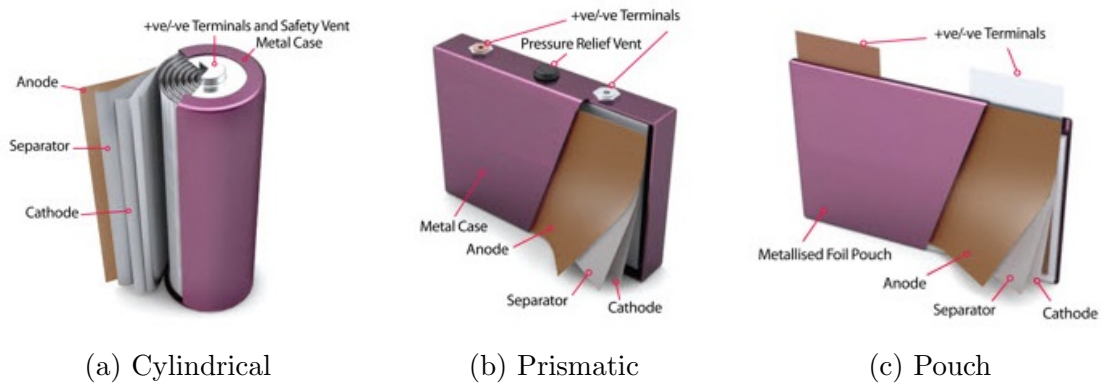


Figure 2.6: Li-ion cell form factors [23,24].

important, and is thus a necessary step in increasing pack-level energy density [25]. Due to the layered nature of the cell construction, thermal conductivity is greatly reduced along the radial direction in cylindrical cells and cross-plane (through the thickness) in prismatic and pouch cells.

2.2 Fast Charging Infrastructure

As manufacturers continue to develop higher-capacity battery packs with support for further-reduced charging times, additional charging infrastructure must be developed with increased power delivery capabilities. Tesla has recently introduced a new charging architecture, bringing power levels up to 250 kW [26] and Porsche has also unveiled charging stations aimed at fast charging, offering power levels up to 350 kW [27]. Open networks are also being deployed with broad support for fast charging. One such network is Electrify America, which has deployed a vast network of 350 kW chargers across the United States [28].

2.3 Prior Art

With the increasing commercial viability of EVs and the potential for fast charging to alleviate common concerns among consumers, there has been significant research interest in increasing charge rates. This section is intended to provide a brief overview of the prior art in this area.

2.3.1 Battery Cell Loss Modelling

An estimate of energy loss (i.e. internal heat generation) of the cells is a critical input to any physics-based thermal modelling. Energy loss in Li-ion cells may be divided into reversible (entropic) and irreversible (Joule) components [10, 29–33]. Simplified models may be developed by considering only Joule heating, at the expense of model fidelity. Both reversible and irreversible heating effects are considered in this thesis.

The reversible heat generation is a result of entropy change in the cells and can be estimated using either the potentiometric method or the calorimetric method [29, 30]. Under the potentiometric method, the reversible heat generation is modelled using the cell's entropic heating coefficient, which is the rate of change of the cell open-circuit voltage with respect to temperature. The entropic heating coefficient is a function of state-of-charge and temperature and is an electrochemical characteristic of the cell. The reversible losses are modelled as the product of the entropic heating coefficient the current, and the temperature expressed in absolute terms [10, 30–32, 34]. It must be determined for each different model of cell [29, 35]. Under the calorimetric method, the reversible heat generation is estimated by measuring the

total heat generation for a charge and discharge cycle. Assuming that the irreversible losses are identical for both cases, the difference in heat generation can be attributed to the reversible losses [30].

The irreversible heat generation is caused by deviation of the cell's terminal voltage from its open-circuit voltage due to electrochemical polarization, resistive loss in the electrode and other factors. There are several methods for estimating the irreversible losses, including by known voltage-current characteristics, by comparing cell voltage to OCV, by intermittent charging and discharging, and by measuring resistance with an alternating current (AC) impedance meter [11].

Whereas the reversible heat generation can be either positive (exothermic) or negative (endothermic), the irreversible heat generation is always positive. While a model of internal heat generation considering reversible and irreversible contributions is fairly straightforward to implement, characterization of the entropic heating coefficient requires quantifying extremely minor changes in OCV. Existing literature on the topic of entropic heating coefficient characterization is limited. Authors in [29] developed an entropic heating coefficient map for a lithium iron phosphate (LFP) cell using a test grid consisting of 21 SOC points and 15 temperature points from 55 °C to -20 °C. Nine cells are tested in parallel to accelerate the test, cells are discharged to test points at a rate of C/10 and a four-hour soak time is allowed following each discharge. The need to account for self-discharge of the cell is noted but not discussed in any detail.

2.3.2 Battery Thermal Modelling

Detailed and accurate knowledge of the temperature distribution inside a battery pack allows the manufacturer to extract maximum performance, reliability, and longevity from their components. Design of the battery pack and cooling strategy to maintain temperature uniformity is a crucial step toward support for higher charge rates [10]. Sophisticated, three-dimensional thermal models can be used during design to refine the cooling and charging processes. Simplified reduced-order models can be deployed online, increasing the resolution of estimated temperature distribution while reducing the number of embedded sensors [13]. This may be very beneficial, as there are few temperature measurement requirements mandated in the battery packs of production EVs [36] and each additional sensor represents a large incremental cost. Furthermore, while a temperature sensor may be placed on the surface of a cell, it is not feasible to measure the internal temperature, though it may be obtained from a thermal model.

Thermal modelling of battery cells is typically conducted using numerical modelling (i.e. CFD), though neural networks (NNs) are increasingly being applied to this task. CFD-based approaches rely on a detailed understanding of the underlying physics, component composition, material properties, and electrochemical characteristics to develop a set of governing equations, which is then solved numerically [37]. Though costly to develop and execute, these models can be used to evaluate various designs in the absence of a physical prototype or test fixture. Neural networks bypass the need for such an understanding of the physics and components by observing the

interaction between model inputs and output based on previously collected experimental data. Neural networks may be employed to predict cell and pack temperatures without the need for explicit loss modelling, as this may be built-into the NN model through the input variables. These models require careful selection of inputs and a large database of training data; they are costly to develop but subsequent simulations are computationally inexpensive. Due to their dependence on experimental data, NN-based models are not appropriate for evaluation of preliminary designs.

CFD-Based

The topic of battery cell and module thermal modelling using CFD has seen much discussion, though only a small fraction with a focus on fast charging.

In [38], a thermal model is developed using CFD for a Li-ion pouch cell and employed for discharge rates up to 5C. Importantly, this work also considers local variations in heat generation caused by non-homogeneous current density. This typically results in increased temperatures near the cell tabs, and more significant temperature gradients. Thermal modelling results in this work are validated using experimental data, and modelled temperatures appear to show good agreement with test data.

Thorough CFD analysis is critical in the design of a battery pack. Design parameters of a mini-channel cold plate are investigated using CFD in [39], comparing battery cooling performance during discharges up to 5C. Simulations are used to quantify decreasing battery temperatures with increasing flow rate and number of channels, however, this work does not consider non-isotropic thermal conductivity

in the battery cells and no experimental validation is presented. Non-linear optimization techniques are employed in [40] to determine cold plate designs which *independently* minimize the average temperature of the cold plate surface, the temperature deviation of the cold plate surface, and the coolant pressure drop within the cold plate. The cold plate designs minimizing the *average* temperature and the pressure drop were found to be similar, both of which were characterized by cooling channels occupying the greatest-possible area inside the cold plate. Authors in [41] employ a CFD model in the design exploration of a cold plate. The thermal model is used to evaluate the effectiveness of different channel designs and the impact on temperature distribution and pressure drop. For the proposed designs, it is found that there is little benefit of increasing the number of cooling channels in the plate beyond five, and that inlet coolant temperature has little impact on standard deviation of temperature on the cell face.

Neural Network-Based

In [42], a neural network is used to predict temperatures of a prismatic LFP cell during charging at 1C and discharging at 2C and 4C rates in a laboratory setting. The Levenberg–Marquardt training algorithm is used and inputs to the model are limited to ambient temperature, cell current, remaining battery capacity. The sole output from the model is a single temperature value to represent the face of the cell. Notably, this model does not consider cell temperature at past time steps, nor does it consider any temperature variability on the cell face. Despite this, the model is able to show good agreement with the measured data.

Fang et al. [43] employ a back-propagation neural network to predict the surface temperature of a nickel-metal hydride battery under different charge rates and ambient temperature conditions. The authors reported a good level of agreement between the model and experimental results.

2.3.3 Battery Thermal Management Solutions

Thermal management solutions for EV batteries may utilize air or liquid cooling, or in extreme cases, two-phase cooling solutions. It is important to size the thermal management system carefully, as excessive cooling capacity only adds to the mass of the vehicle. Liquid cooling solutions are well-suited to fast charging EV applications due to their balance of cooling ability and complexity. Two-phase cooling solutions, such as [44], add a great deal of design complexity and risk thermal runaway in the event of dryout of the liquid phase. In the event of dryout, the ability of the system to remove heat from the cells drops dramatically, resulting in rapid temperature rise of the cells.

Liquid cooling of pouch cells typically employs cold plates, either placed between the cells themselves or at the sides of the cells, with additional plates between the cells to draw heat from the cell face toward the cold plate. An example of a cold plate placed directly between cells shown in Figure 2.7.

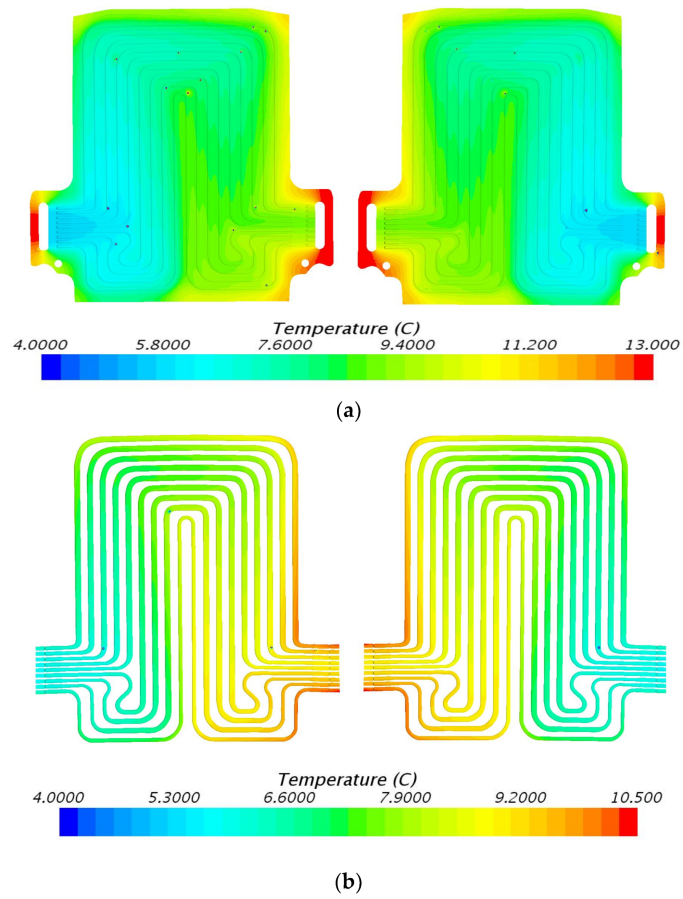


Figure 2.7: Pouch cell cold plate design [45], showing plate temperatures (top) and coolant temperatures (bottom).

An example of a cooling strategy for cylindrical Li-ion cells is the battery pack of a Tesla Model S, which uses a “wavy profile” cooling tube to increase contact with the cylindrical cells, as shown in Figure 2.8.

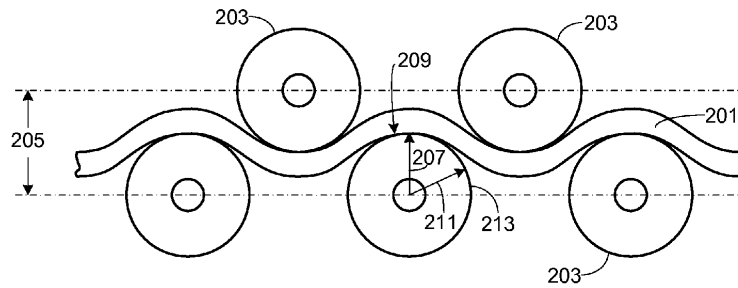


Figure 2.8: “Wavy profile” cooling tube used in Tesla battery packs [46].

This figure shows a small cross-section of a battery module. Elements labeled “203” represent the cylindrical cells and the cooling tube is labeled “201”. Thermal modelling in [47] found this type of cooling configuration to be effective even at charge rates up to 5C; it should be noted, however, that this study treated the cells using lumped system analysis, thereby neglecting temperature gradients inside the cells.

2.3.4 Fast Charging Implementation

Authors in [48] achieved higher charge rates while mitigating cell ageing caused by lithium plating by instrumenting a test cell with a third, or “reference”, electrode, and monitoring the voltage between the negative terminal and the reference terminal. Though the authors point out that this method cannot be directly applied to commercial cells due to the lack of reference electrode, a charging current map is proposed and transferred to the pack level. Implications of high-rate charging on cell ageing are also explored in [49], and it is found that fast charging can be achieved without significant sacrifice in cell health or charging efficiency by considering the charging protocol.

In [50], a thermal management system design is proposed and constructed for a test module housing Li-ion pouch cells. Cold plates are used to remove heat via the sides of the pouch cells. The process of cell selection and pack geometry exploration are not discussed, and only charge rates up to 3C are considered.

Fast charging is also beginning to see commercialization in EVs. The Porsche Taycan, first available in 2019, offers charging at up to 270 kW. The Taycan uses 65 Ah pouch cells which form an 800 V pack. This high voltage pack reduces Joule losses, which increase with the squared current and are therefore a significant consideration at higher power levels. With a peak charging current of 334 A and a pack consisting of two parallel arrangements of 198 series-connected cells [51], the peak charge rate of the Taycan equates to approximately 2.6 C. Peak charging power of the Taycan has been promised to increase to 350 kW in the year 2021 [52].

Chapter 3

Cell Testing and Selection for Fast Charging

This section examines four different battery cells, with the intention of capturing a range of cell chemistry and characteristics. The battery cells and the equipment used in testing are first outlined, and the candidate cells are characterized and tested for a series of fast charges at rates up to 5C and 10C. From the experimental data and using simplified thermal models, an inter-cell cooling plate is sized for each cell to enable comparison of energy density in a pack. Different cooling configurations are compared and a cell is selected for implementation in a fast charging module. All tests are performed inside an environmental chamber, which is used to maintain a consistent temperature throughout testing.

3.1 Specifications of Cells Tested

Specifications for the four cells tested are listed in Table 3.1, where the nominal resistance and power density are calculated at 50% SOC from hybrid pulsed power characterization test data [53].

Table 3.1: Battery cell specifications.

Manufacturer, Model	A123, AMP20M1HD-A	Turnigy, Graphene 65C	Kokam, SLPB78216216H	A123, AMP26 NMC
Chemistry	LiFePO4 (LFP)	NMC/NCA ¹	NMC	NMC
Size [mm]	160 x 227 x 7.25	49 x 135 x 9	226 x 227 x 7.8	161 x 227 x 7.5
Rated Capacity [A h]	20	5.0	31	26
Nominal Resistance [$m\Omega$]	2.6	2.9	2.4	2.7
Mass [g]	496	140	720	550
Power Density [$kW kg^{-1}$]	1.6	8.0	1.7	2.0
Energy Density [$Wh kg^{-1}$, $Wh l^{-1}$]	131, 247	136, 317	158, 284	180, 361

¹ Not specified on data sheet. The chemistry of the Turnigy cell is assumed to be lithium nickel manganese cobalt oxide (NMC) or lithium nickel cobalt aluminum oxide (NCA) based on the voltage range of the cell and its nominal voltage.

Though high charge rates have been achieved with NMC cells in lab testing [54], the rate capability of this chemistry has not been fully investigated in commercial cells. It should also be noted that the Turnigy cell is much smaller than the other cells studied here, which may allow for greater flexibility in packaging compared to larger cells. The increased thickness of the Turnigy cell, however, is expected to reduce its ability to dissipate heat through its surface. From Table 3.1, it can also be seen that the Turnigy cell has the highest power capability of all four cells, indicating suitability for fast charging.

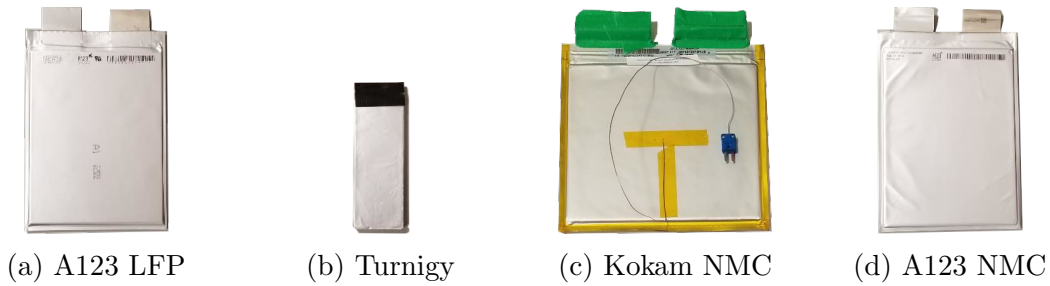


Figure 3.1: Battery cells tested.

3.2 Equipment and Experimental Setup

Laboratory tests are conducted with the cells inside a Thermotron Industries SE-3000-6-6 environmental chamber, which is used to maintain an ambient temperature of 20 °C throughout testing. Cell cycling and data logging are accomplished using a Digatron Power Electronics MCT 75-0/5-8ME cell cycler, with voltage sensing accuracy of 5 mV for the 0–5 V voltage range. Specifications of the cell cycler and environmental chamber are presented in Table 3.2 and Table 3.3, respectively.

Table 3.2: Battery cell cycler specifications.

Manufacturer	Digatron Power Electronics
Model Number	MCT 75-0/5-8ME
Voltage Range	0 to 5 V
Number of Channels	8 at 75 A each
Voltage Accuracy	$\pm 0.1\%$ of full scale
Current Accuracy	$\pm 0.1\%$ of full scale

Table 3.3: Environmental chamber specifications.

Manufacturer	Thermotron Industries
Model Number	SE-3000-6-6
Internal Dimensions	1.21m x 1.82m x 1.32m
Temperature Accuracy	± 0.3 °C
Temperature Uniformity	± 0.7 °C

When required, currents exceeding the 75A rating of the individual channels are achieved by connecting multiple channels in parallel. Using all channels simultaneously, currents up to 600 A can be achieved.

3.3 Cell Characterization

The cells are charged at a series of increasing rates, up to the selected limit for each cell. The testing is performed with parallel-connected, 75 A, 0 to 5 V, 0.1% accuracy channels of the Digatron Power Electronics Universal Battery Tester system. Prior to each charge, cells are slowly discharged at a rate of C/2 until the selected voltage cut-off, which correlates to about 10% SOC: 3.2 V for the A123 LFP cell and 3.5 V for the Turnigy, Kokam, and A123 NMC cells. After a 30-minute rest period, each cell is charged using a constant-current, constant-voltage (CC-CV) protocol. Under this protocol, the specified C-rate is maintained for the constant current portion of the charge until the upper voltage limit is reached: 3.6 V for the A123 LFP cell, 4.2 V for the Turnigy, Kokam, and A123 NMC cells. Once this limit is reached, the current begins to decrease in order to maintain a constant voltage; the charge is considered to be complete when the current falls below 0.1 A. Following another

30-minute rest period, the discharge and charge steps are repeated for a second time at the same C-rate so that a charge efficiency can be accurately calculated. The entire process is then repeated for the remaining C-rates prescribed in the test plan.

Table 3.4: Charge protocol for cells over charge-rate range.

Step	Action	Step End
I	Pause	After 30 minutes
II	C/2 Discharge 1	$V < V_{cut-off}$
III	Pause	After 30 minutes
IV	CC-CV Charge 1	$I < I_{cut-off}$
V	Pause	After 30 minutes
VI	C/2 Discharge 2	$V < V_{cut-off}$
VII	Pause	After 30 minutes
VIII	CC-CV Charge 2	$I < I_{cut-off}$
IX	Repeat steps I–VIII	A123 and Kokam: 1C, 2C, 3C, 4C, 5C Turnigy: 1C, 2C, 4C, 6C, 8C, 10C

3.3.1 Measured Cell Data for a Range of Fast Charge Rates

For each battery cell, measured terminal voltage and current for all charge rates tested are presented in Figure 3.2, where the calculated OCV is shown to illustrate the over-potential for each charge rate. Because of its higher rate capability, the Turnigy cell is tested at charge rates up to 10C, while the other cells are tested at charge rates up to 5C. As is characteristic of the CC-CV charge profile, cell voltage limits are reached at lower SOC values as the charge rates are increased, triggering earlier transition to constant voltage charging.

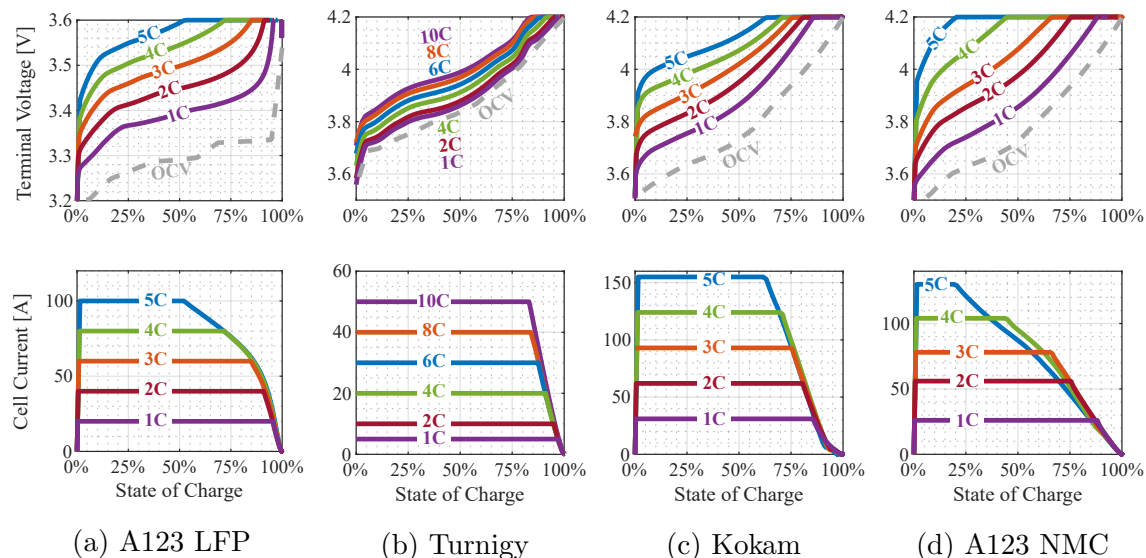


Figure 3.2: Measured fast charge data for each cell type.

3.3.2 Cell Performance as a Function of Charge Rate

Using the fast charge data, the performance of each cell can be evaluated and compared. Three metrics are used to compare the fast charging performance and the response to increasing charge rates across the different cells: the charging efficiency, the SOC at transition from constant-current to constant-voltage charging, and the cell resistance normalized to its 1C value (or 2C value, in the case of the Turnigy cell). These metrics are evaluated for the four cells and presented in Figure 3.3. The charging efficiency is shown in Figure 3.3a, it represents the portion of energy that is added to the cell, and not lost as heat to the environment. Higher charging efficiencies indicate lower losses for a given charge rate, and therefore less waste heat to be removed from the battery pack, which reduces the requirements of the thermal management system. It can be seen that the Turnigy cell has a much higher charging

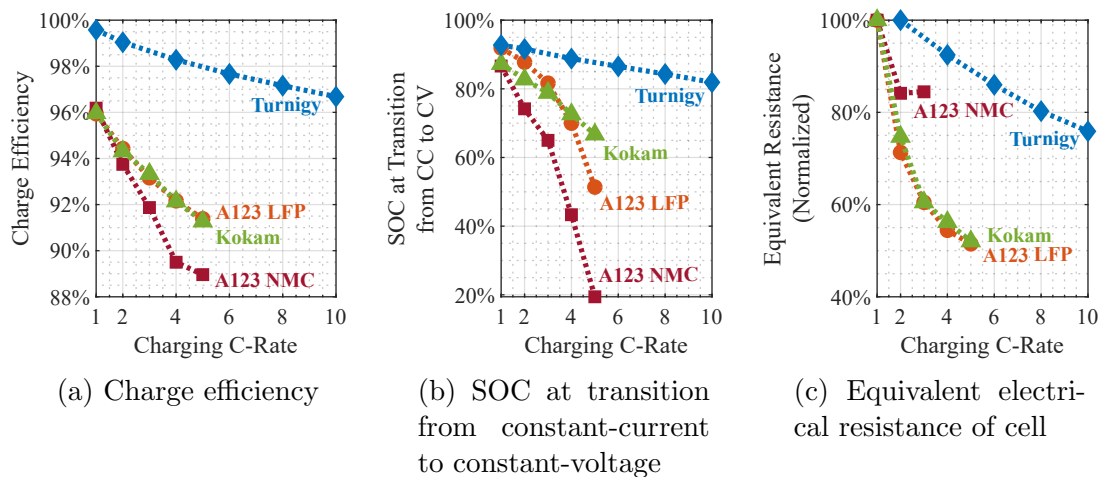


Figure 3.3: Fast charge performance as a function of charge rate.

efficiency than the other cells tested, and its efficiency decreases very little as the charge rate increases. The A123 NMC cell has the lowest charging efficiency, and the most dramatic decrease with increasing charge rate.

The SOC at transition from constant-current to constant-voltage charging is shown in Figure 3.3b. The higher the value of this metric, the longer the prescribed charge rate is sustained. This ultimately results in a faster CC-CV charge, since the higher current is sustained for longer. For the charge rates tested, the Turnigy cell is consistently able to reach a high SOC (above 80%) before this transition—while the A123 cell drops from transitioning at over 80% SOC for a 1C charge to approximately 20% SOC for a 5C charge. This suggests that the A123 does not respond well to CC-CV charging at higher charge rates.

Figure 3.3c shows the normalized equivalent electrical resistance as a function of charge rate, which is determined by calculating the fixed resistance value which creates the loss observed for a given charge rate. For each cell, the normalized

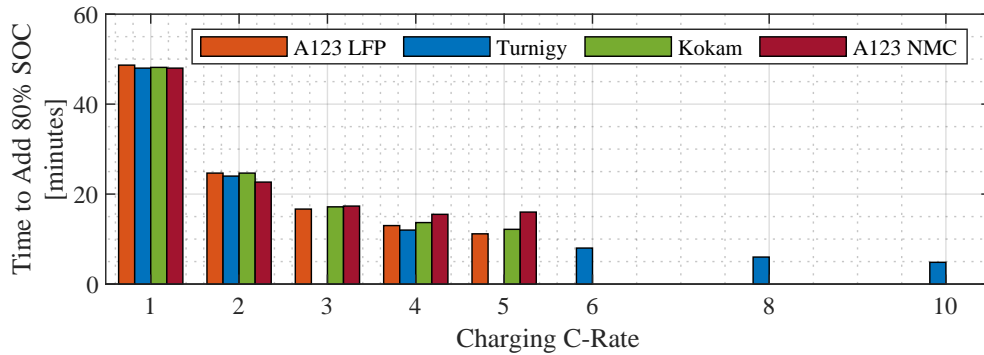
equivalent resistance is obtained by dividing by its 1C charging resistance. The normalized equivalent resistance shows that resistance is non-linear at high charge rates—similar to the non-linear Butler-Volmer equation resistance, which is often observed for batteries at low temperatures [55].

From the plots presented in Figure 3.3, the Turnigy cell appears particularly well-suited for ultrafast charging, while the A123 NMC cell appears to be the least suitable of the cells tested. The A123 LFP and Kokam NMC cells fall in the middle, though they do not perform as well as the Turnigy cell, they are much more suitable for fast charging than the A123 NMC cell.

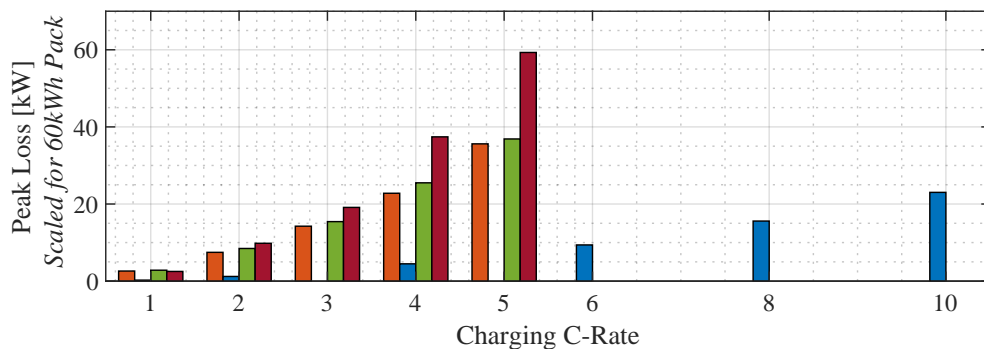
3.3.3 Pack Performance as a Function of Charge Rate

In Figure 3.4a, the measured time to add 80% SOC is plotted for each cell and charge rate, showing time required to fast charge an EV battery pack for each case. The peak cell loss is also calculated by assuming the measured, cumulative charging loss is distributed over the charge as a function of the squared current. The peak cell loss is then scaled for a 60 kW h pack and plotted in Figure 3.4b.

Figure 3.4a shows that, for the A123 NMC cell, increasing the constant-current charge rate from 3C to 4C only reduces the time to add 80% SOC by one minute. Furthermore, increasing from 4C to 5C yields no significant time savings for the A123 cell, which is also associated with a 60% increase in peak loss, as shown in Figure 3.4b. In these plots (and consistent with Figure 3.3), the Turnigy cell is a clear outlier: as the charge rate is increased, the time to add 80% SOC decreases steadily and the peak losses remain low for the charge rates tested. Figure 3.4b also shows



(a) Experimentally measured time to add 80% SOC.



(b) Peak charging loss scaled to a 60 kWh pack.

Figure 3.4: Comparison of fast charging time and pack loss.

that peak battery pack loss can be very high, in the range of 20–60 kW for charge rates of 4C or 5C. Removing this amount of heat from a vehicle’s battery pack and transferring it to the surroundings is one of the key challenges of ultrafast charging.

3.4 Required Cooling System Size Comparison

Simplified, three-dimensional thermal models are used to compare the size of the cooling system required for each of the four cells, allowing for a more equitable

comparison. For each of the four cells studied, the thickness of an aluminum inter-cell cooling plate is varied to adjust the cooling capability as needed. Increasing the plate thickness increases the cooling capability of the module, but decreases the gravitational and volumetric energy and power densities of the pack. Cooling is provided by cold plates (at this stage, represented as a fixed-temperature wall) at both sides of the cell, in contact with the inter-cell cooling plates. This model is shown in Figure 3.5.

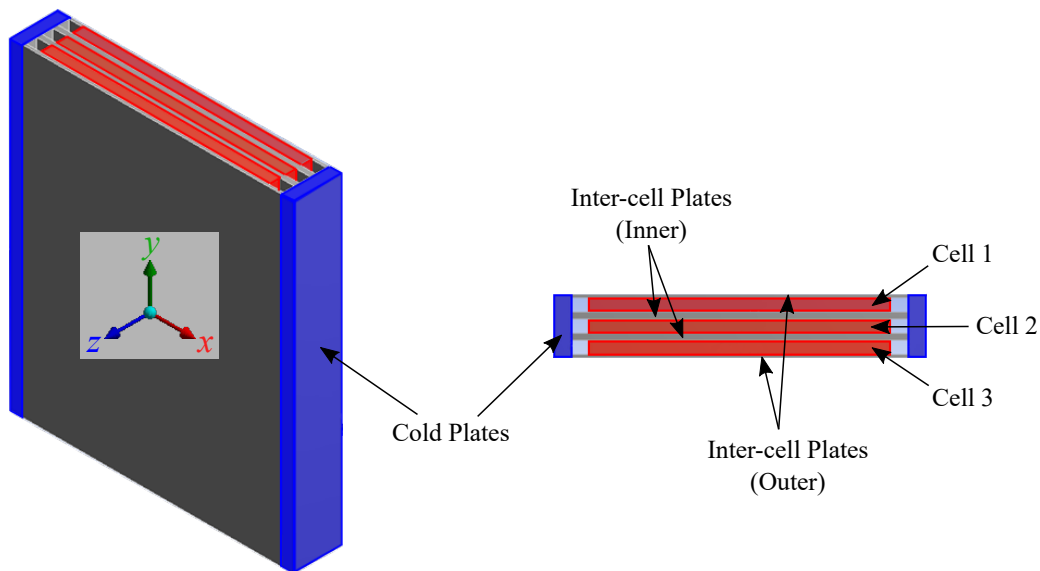


Figure 3.5: Simplified, three-dimensional thermal model, before applying symmetry planes.

These models are built in ANSYS Mechanical using the Transient Thermal functionality. For each cell, the required inter-cell cooling plate thickness is determined. Despite the idealized cooling system, this thermal model provides a means of comparison for the heat generated in each of the cells and their ability to reject heat through their surface.

3.4.1 Thermal Model Properties and Boundary Conditions

Thermal properties are obtained directly from literature, or by scaling literature values by density ratio where necessary. Properties for all materials used in the thermal modelling are presented in Table 3.5.

Table 3.5: Simplified thermal model properties.

Domain	Density [kg m^{-3}]	Heat Capacity [$\text{J kg}^{-1} \text{K}^{-1}$]	Thermal Conductivity [$\text{W m}^{-1} \text{K}^{-1}$]	
			In-plane (x, y)	Through-plane (z)
A123 LFP ¹	1884	610	16.4	0.51
Turnigy ²	2333	1054	28.8	1.33
Kokam ²	1799	813	22.2	1.03
A123 NMC ²	2007	907	24.8	1.15
Aluminum	2689	951		237.5

¹ Published thermal property values [56, 57].

² Scaled by density ratio from published values for similar cells [50].

The method of heat removal (cold plates at the ends of the module) in the model is approximated as a constant-temperature wall, uniform and fixed to 20 °C, adjacent to the aluminum inter-cell cooling plates, and connected using aluminum bars to increase contact. The single heat source in the model is the internal heat generation of the battery cell. During each fast charge and for each cell, the instantaneous heat generation is determined by scaling the total energy lost after a charge and discharge of equal capacity (net-zero charge cycle); the total energy loss measurement is distributed throughout the charge according to the square of the instantaneous current. This yields the heat generation rate as a function of charging time. In essence, this method of modelling the heat generation throughout the charge relies on the approximation that the cell resistance is constant for the net-zero charge cycle.

3.4.2 Thermal Modelling Results

Figure 3.6 shows the predicted temperature rise with varying inter-cell plate thickness for each of the four cells. This study is used to identify the required cooling system size for each cell. The parameter p is introduced to denote the inter-cell cooling plate thickness normalized to the cell thickness, therefore if $p = 0.1$, the inter-cell cooling plate thickness is 10% of the cell thickness. This parameter allows for the cooling requirements to be effectively compared across the different cells.

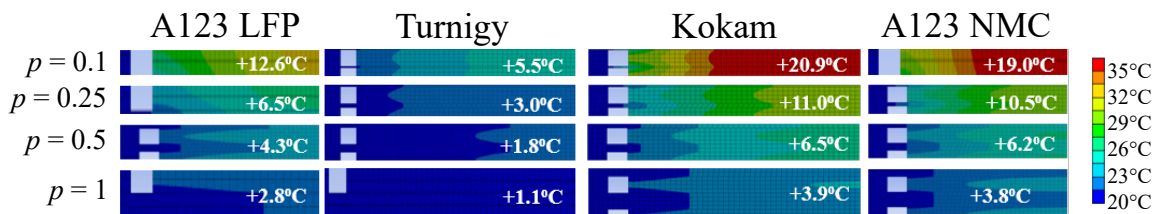


Figure 3.6: Predicted temperature rise versus cooling method and inter-cell cooling plate thickness p for a 4C charge rate case.

As shown in Figure 3.6, the Turnigy cell can be cooled effectively using much less material than the other cells, leading to higher effective energy density. Even for $p = 0.1$, the peak temperature of the Turnigy cell is maintained at a safe level, while the Kokam and A123 NMC cells will likely require $p > 0.1$. For the A123 cells the additional cooling capability of the $p = 0.5$ inter-cell plate is deemed to be minimal compared to the increased module weight. For the A123 LFP cell, during a 4C charge, there was only a 2 °C difference in peak temperature between the $p = 0.25$ and $p = 0.5$ inter-cell plates. Further, for the A123 NMC cell, which produces nearly double the loss of the LFP cell, this difference was only 6 °C.

3.4.3 Double-sided versus Single-sided Cooling

Placement of the cold plates is also investigated in order to determine the configuration which provides more effective and more uniform cooling. Three different configurations are modelled: (1) cold plates placed on either side of the cells (double-sided), (2) a single cold plate placed on one side of the cells (single-sided), and (3) a single cold plate placed at the bottom of the cells (bottom-only). These configurations are shown in Figure 3.7 for the A123 NMC cell with $p = 0.5$. In the first configuration, the tops of the cells should see the largest temperature rise as they have the longest path to the cold plate. In the second configuration, the cells see a large temperature rise on the side opposite cold plate. Like the first configuration, heat must be transferred across a greater length in order to be removed, making these configurations less effective and less conducive to uniform cooling. With two cooling plates, heat can be removed much more effectively and uniformly, though this is at the expense of increased size and weight of the battery pack. For the A123 NMC cell, Figure 3.8 shows the modelled temperature rise as a function of cold plate placement and inter-cell plate thickness, p .

For the A123 NMC cell shown in Figure 3.7, the bottom placement yields the worst performance, with a maximum temperature rise of 35 °C compared to just 6 °C for the two-sided configuration. For the Turnigy cell, the bottom placement yields a temperature rise similar to the two-sided configuration. This can be attributed to the difference in size and thermal conductivity between the Turnigy cell and the A123 cells; importantly, the A123 cells are twice the length of the Turnigy cell. Since the thermal resistance increases as the thermal path becomes longer, placement of

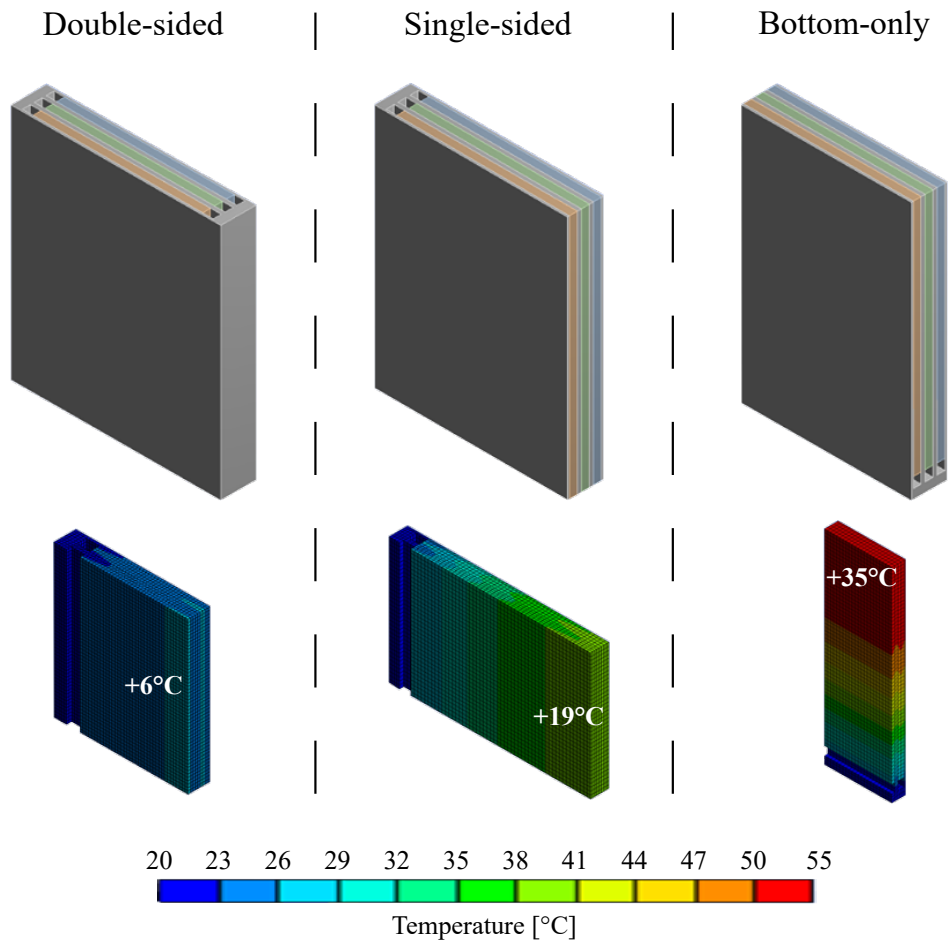


Figure 3.7: Temperature *rise* for 4C charge versus cooling plate placement for A123 NMC cell with $p = 0.5$ plate thickness.

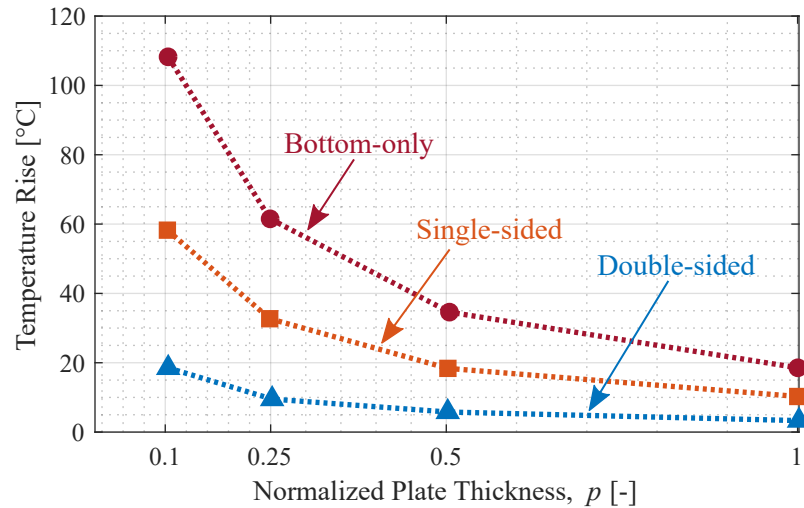


Figure 3.8: Temperature *rise* for 4C charge versus cooling plate thickness and placement for A123 NMC cell.





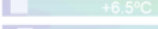

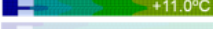
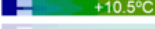







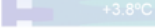
the cold plate is more important for cell with a higher aspect ratio. According to the properties listed in Table 3.5, the thermal conductivity, both in-plane and through-plane, of the Turnigy cell is significantly higher than that of the A123 cells and the Kokam cell. For the Turnigy cell, this high thermal conductivity means that one plate at the bottom of the module is able to provide sufficient cooling and maintain the peak temperature to within an acceptable range.

3.4.4 Comparison of Cell and Cooling System Options

The components of the thermal management system greatly impact the energy and power densities attainable at a pack level, with significant implications to the driving range and charging power levels of the EV. For this reason and many others, it is important to select an appropriate cell and to not oversize thermal management

system. A cell which generates less heat or dissipates heat more easily can be paired with a less invasive thermal management system. The effective energy density is introduced to take into account the increased mass and volume of a battery pack from the inter-cell plates. It is calculated by dividing the total energy in a cell by the sum of the inter-cell plate and cell mass (for gravimetric energy density) or volume (for volumetric energy density). The effective energy density, therefore, enables a direct comparison of the different cells and their thermal management requirements in a pack. Taking the A132 NMC cell as an example, increasing the inter-cell plate thickness from $p = 0.1$ to $p = 0.25$ yields a decrease in effective energy density of 16%. The effective energy density corresponding to the selected inter-cell plate thickness for each cell is presented in Table 3.6.

Table 3.6: Selected plate thickness, p , and comparison of selected cell and cooling system options.

	A123 LFP	Turnigy	Kokam NMC	A123 NMC
$p = 0.1$	 +12.6°C	 +5.5°C	 +20.9°C	 +19.0°C
$p = 0.25$	 +6.5°C	 +3.0°C	 +11.0°C	 +10.5°C
$p = 0.5$	 +4.3°C	 +1.8°C	 +6.5°C	 +6.2°C
$p = 1$	 +2.8°C	 +1.1°C	 +3.9°C	 +3.8°C
Plate thickness p selected for $< 15^\circ\text{C}$ rise	0.1	0.1	0.25	0.25
Energy Density, Cell Only	131 W h kg ⁻¹ 247 W h l ⁻¹	136 W h kg ⁻¹ 317 W h l ⁻¹	158 W h kg ⁻¹ 284 W h l ⁻¹	180 W h kg ⁻¹ 361 W h l ⁻¹
Effective Energy Density, Cell and Inter-cell Cooling Plate	113 W h kg ⁻¹ 222 W h l ⁻¹	120 W h kg ⁻¹ 285 W h l ⁻¹	112 W h kg ⁻¹ 223 W h l ⁻¹	131 W h kg ⁻¹ 283 W h l ⁻¹

Despite having a lower effective energy density than the Turnigy and A123 NMC cells, the Kokam cell is selected for implementation in a fast charging test module due to its packaging, which is more favourable for implementation in the battery

pack of an EV. The far lower capacity of the Turnigy cell (5 A h versus 31 A h for the Kokam cell) means that many cells would be required to build a battery pack of a given capacity, which would result in a more complex design. The capacity and form factor of the Kokam cell make it the most suitable for implementation in the battery pack of an EV. Chapter 4 is concerned with the development of a fast charging test module; since temperature uniformity within the cell is of utmost importance during fast charging [58,59], two cold plates are used for the module.

Chapter 4

Experimental Inter-cell Cooling Module

To facilitate fast charging tests, an experimental test module is built to house three Kokam NMC cells connected in parallel, each separated by a solid aluminum plate (inter-cell cooling plate). The module is designed based on the analysis in Chapter 3, with an inter-cell cooling plate thickness of $p = 0.25$. Active cooling is provided by two aluminum cold plates, one at either side, through which a cooling fluid is circulated. The cell cycler and environmental chamber detailed in Section 3.2 are used to facilitate tests of the module.

4.1 Geometry and Design

The module is intended to replicate the model used in the previous analysis. Inch-thick plastic is used at the outside faces of the test module to render the heat loss

through these surfaces negligible and emulate an infinitely long stack of cells. Thermal pads are used at the interface of the cells and the inter-cell aluminum plates to enhance heat transfer from the cells to the plates. The outermost inter-cell aluminum plates are half of the thickness of the interior plates—as is the case in the model—to ensure uniform cooling, as these plates only contact the face of one cell, instead of two. At either side of the module, the inter-cell aluminum plates are fixed to the cold plates using aluminum bars. These aluminum bars enhance contact between the inter-cell plates and the cold plates. In order to reduce contact resistance in the module, all metallic mating surfaces are milled to improve flatness and thermal paste is applied at all metal-on-metal connections. Thermal properties of the materials used in the module are presented in Table 4.1.

Table 4.1: Thermal properties of the materials used in the test module.

Component	Material	Density [kg m^{-3}]	Heat Capacity [$\text{J kg}^{-1} \text{K}^{-1}$]	Thermal Conductivity [$\text{W m}^{-1} \text{K}^{-1}$]
Inter-cell Plate	Aluminum 3003-H14	2800	900	180
Bar	Aluminum 6061-T6511	2700	900	170
Thermal Pad	Tflex HR440	-	-	1.8
Plastic	UHMW Polyethylene	940	1750	0.41

Once assembled, the cells are compressed using studs fed through the plastic and the inter-cell aluminum plates. Based on the analysis in Chapter 3, the plate with 25% of cell thickness ($p = 0.25$) is chosen for the aluminum inter-cell plates in the test module, since it provides a reasonable compromise between temperature rise and effective energy density. In application, 12-gauge aluminum is used for the inter-cell plates, which equates to $p = 0.26$ for the Kokam cell. Dimensions of test module

components are provided in Table 4.2.

Table 4.2: Dimensions of test module components.

Component	Dimensions [mm]
Inter-cell plate, inner	$279 \times 254 \times 2$
Inter-cell plate, outer	$279 \times 254 \times 1$
Bar	$279 \times 19 \times 9.5$
Plastic	$279 \times 254 \times 25$

With the efforts taken to reduce contact resistance in the module, the numerical analysis assumes a negligible contact resistance between the bars, inter-cell plates, and cold plates. The cooling fluid used is an ethylene glycol-water solution with the properties presented in Table 4.3.

Table 4.3: Properties of ethylene glycol-water solution [60].

Density	1082 kg m^{-3}
Specific Heat Capacity	$3260 \text{ J kg}^{-1} \text{ K}^{-1}$
Thermal Conductivity	$0.402 \text{ W m}^{-1} \text{ K}^{-1}$
Dynamic Viscosity	$4.87 \times 10^{-3} \text{ kg m}^{-1} \text{ s}^{-1}$

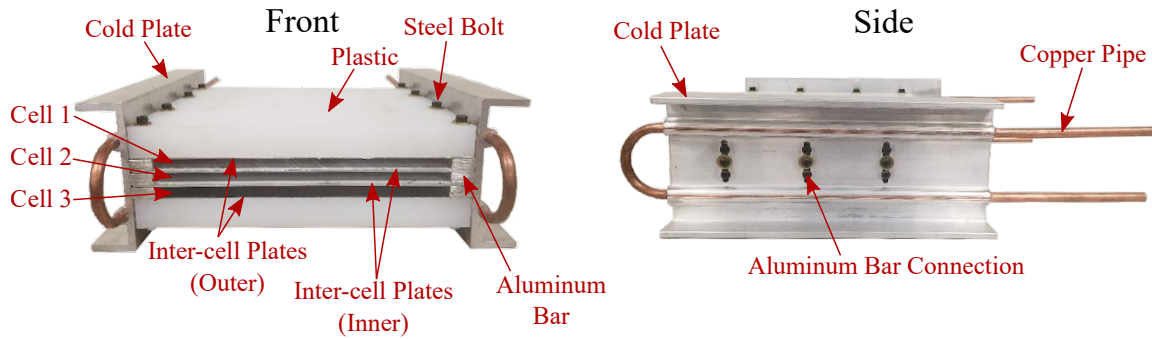
4.2 Component Specifications

Liquid-cooled, aluminum cold plates from Wakefield-Vette (model 180-11-12C) are used in the module. The plates use a rolled-tube design in which 3/8-inch outer diameter copper pipe is attached to the aluminum base. The overall thermal resistance of the cold plates, from the surface of the plate to the inlet water, is specified as $0.041 \text{ }^\circ\text{C W}^{-1}$ for a flow rate of 1.5 GPM ($\approx 5.7 \text{ L min}^{-1}$) [61]. These plates are

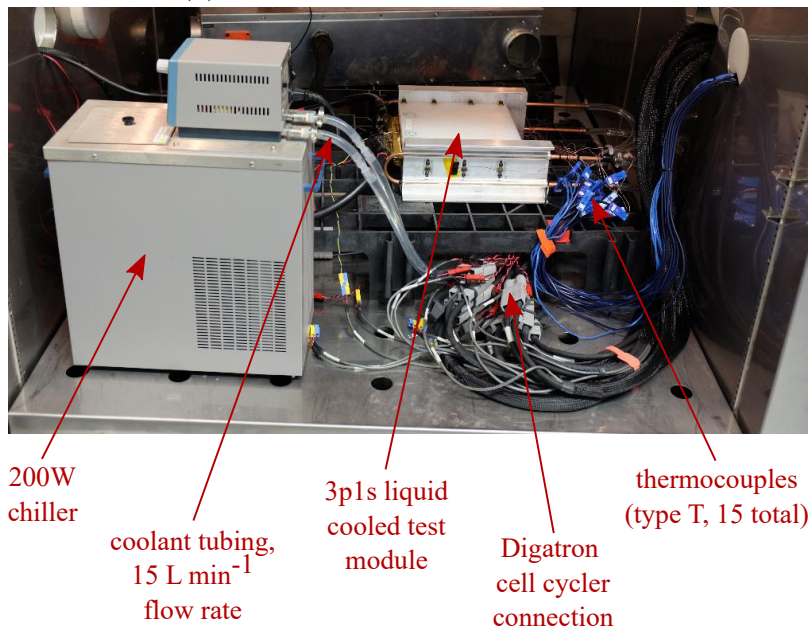
used to approximate the constant temperature boundary condition assumed in the thermal analysis.

A 6 L, 200 W, 1160S circulating bath chiller from VWR International, Inc. is used to provide the cold plates with a constant supply of 20 °C coolant. The chiller is capable of providing coolant from -20 °C to $150\text{ °C} \pm 0.05\text{ °C}$, and employs a two-speed pump with corresponding flow rates of 9 L min^{-1} and 15 L min^{-1} . The higher flow rate is used to better approximate the constant temperature boundary condition.

The test module is shown in Figure 4.1a, and its placement in the environmental chamber is shown in Figure 4.1b.



(a) Prototype 3p1s battery module.

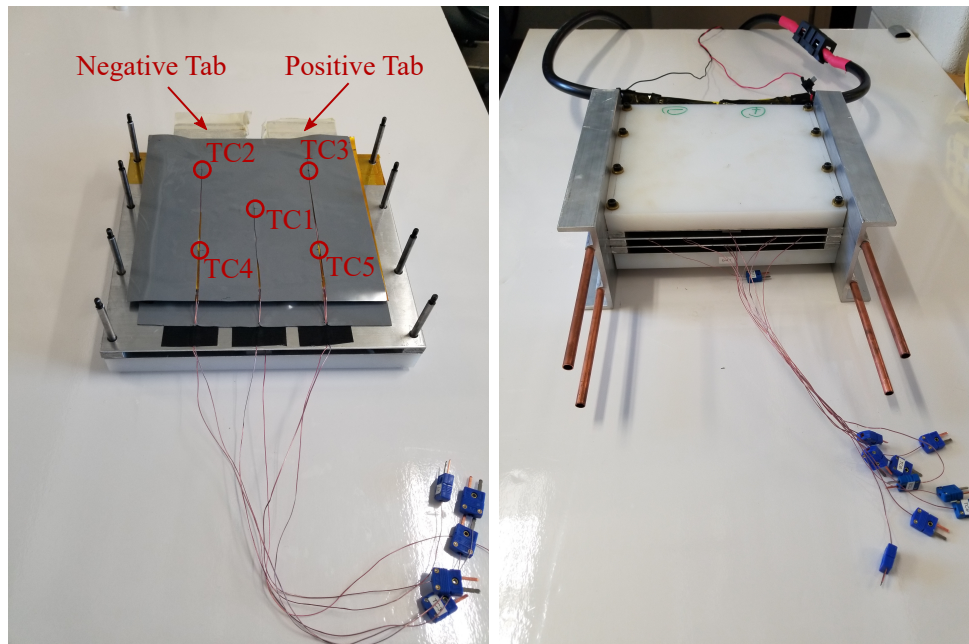


(b) Test setup inside environmental chamber.

Figure 4.1: Prototype 3p1s battery module with $p = 0.26$ cooling plates, and placement in environmental chamber

4.3 Instrumentation

A total of fifteen type T thermocouples are placed throughout the test module. Existing literature has shown that the majority of heat is initially generated near the tabs [62, 63]. To capture the temperature distribution of the cells, five of the fifteen thermocouples are placed on the face of the middle cell—in the positions shown in Figure 4.2a. Of the remaining ten thermocouples, one is placed at the center of the top cell, one at the center of the bottom cell, one on the top inter-cell cooling plate, one at each of the two tabs, one at the coolant inlet and outlet, one on the surface of each cold plate, and one in the surrounding air. The assembled module, with embedded thermocouples, is shown in Figure 4.2b. Data from the thermocouples are captured in LabVIEW using a National Instruments NI-9213 data acquisition system, providing temperature measurements to within 0.7°C.



(a) Middle cell and thermal interface material, with thermocouple locations indicated.

(b) Assembled module, showing connectors of embedded thermocouples.

Figure 4.2: Prototype 3p1s battery module with embedded thermocouples.

Chapter 5

Loss Modelling with Entropic Heating Coefficient

In this chapter, a procedure for experimentally determining the entropic heating coefficient of a Li-ion battery cell is developed, and the result is used to model heat generation within the battery cells.

The entropic heating coefficient is the rate of change of a cell's open-circuit voltage with respect to temperature; it is a function of state of charge and temperature, often expressed in mV K^{-1} . The reversible losses inside the cell are a function of the current, the temperature, and the entropic heating coefficient, which itself is dependent on the cell chemistry. The total cell losses are the sum of the reversible and irreversible losses, where the irreversible losses consist of ohmic losses in the electrodes, ion transport losses, and other irreversible chemical reactions.

The entropic heating coefficient is determined by exposing the cell to a range of

temperatures at each SOC value of interest. The OCV is recorded at each combination of SOC and temperature, and $\partial OCV/\partial T$ is calculated from the measurements. Since a ΔT of 20 °C may result in a ΔOCV of 100 μV or less, it is critical to have a high accuracy and high input impedance voltage sensor. Additionally, the measurement is sensitive to self-discharge of the battery and the amount of time at each test point. A test methodology is developed which achieves an accurate OCV measurement, corrects for self-discharge, and utilizes the minimum necessary soak time. Once determined experimentally, the entropic heating coefficient map is used to model losses during several charges with rates from 1C to 5C, and the results are compared with a constant current loss model derived from experimental data for an NMC cell.

At the peak of total heat generation, the reversible heat generation is observed to contribute up to 23% of the total for a 1C charge, and 9% of the total for a 5C charge. In this work, the potentiometric method is used to estimate the reversible losses and the entropic heating coefficient is determined experimentally. The reversible losses are estimated by comparing the cell terminal voltage to the OCV.

5.1 Battery Cell Loss Model

The reversible and irreversible heat generation inside the cells are estimated using the simplified Bernardi heat generation model [31]. Here, the irreversible heat is estimated by comparing the terminal voltage to the OCV. Equations 5.1 and 5.2,

below, define the reversible and irreversible loss estimates:

$$\dot{Q}_{rev} = -IT \frac{\partial OCV}{\partial T} \quad (5.1)$$

$$\dot{Q}_{irrev} = I(OCV - V_T) \quad (5.2)$$

where I is the current in amperes (defined as positive during discharge), T is the temperature in kelvin, $\partial OCV/\partial T$ is the entropic heating coefficient in $V K^{-1}$, and V_T is the terminal voltage. The resulting \dot{Q} is the loss (internal heat generation) in units of watts.

The total loss is then given by the sum of the reversible and irreversible contributions:

$$\dot{Q}_{total} = \dot{Q}_{rev} + \dot{Q}_{irrev} \quad (5.3)$$

In order to utilize this model, the entropic heating coefficient must first be determined. The terminal voltage, V_T can either be measured or modelled, allowing for the modelling of heat generation during any arbitrary cycle. The subsequent sections are concerned with the measurement of the entropic heating coefficient and utilization of the cell loss model.

5.2 Entropic Heating Coefficient Measurement

Since the entropic heating coefficient test is concerned with very small changes in the battery OCV over very long periods of time, it is necessary to select a voltage sensor with very high resolution. The NI-9239 voltage sensor utilized for the tests

has 24-bit, $1.25\ \mu\text{V}$ resolution which is sufficient for the Kokam cells tested. The cell cycler's voltage sensor—with a resolution of $5\ \text{mV}$ —is used only for the separate hybrid pulse power characterization (HPPC) test which provides the OCV data required to calculate the irreversible losses. Another important concern is the input impedance of the voltage sensor. The $1\ \text{M}\Omega$ -impedance sensor of the data logger is found to discharge the battery cells excessively, given the precision required from the measurement. The cell cycler's voltage sensor exhibits the same problem: with its input impedance of $50\ \text{k}\Omega$, self-discharge would be $0.8\ \mu\text{V h}^{-1}$ for the module studied here, and for a smaller cell with a $3\ \text{A h}$ capacity, it would be $24\ \mu\text{V h}^{-1}$.

In order to reduce unwanted cell discharge through sensor and cycler leads, three LabVIEW-controlled relays are employed using a National Instruments NI-9403 digital input/output module: one for each set of cycler leads (cell cycling and voltage sensing) and one for the data logger leads (voltage sensing). The cycler is connected only when the module must be charged or discharged, and the voltage sensor of the data logger is connected periodically for a predetermined length of time to allow for a reliable measurement. The voltage and temperature data are processed in LabVIEW, which outputs a one-minute moving average of the OCV and thermocouple temperatures. A circuit diagram of the test setup is provided in Figure 5.1.

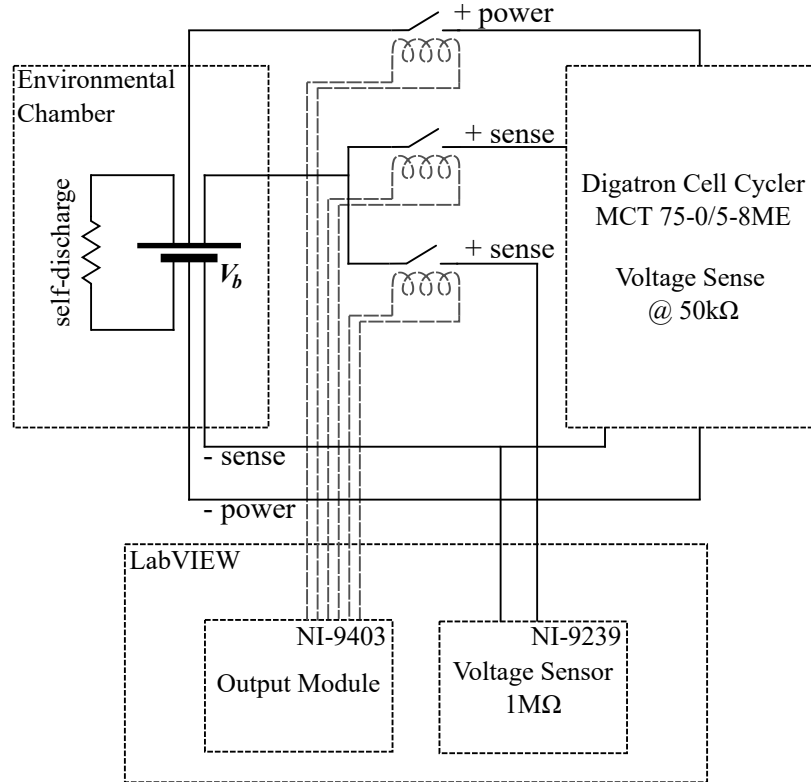


Figure 5.1: Circuit diagram of test setup.

5.2.1 Development of a Test Program

Since the entropic heating coefficient is a function of both the cell temperature and the SOC, the test points form a two-dimensional grid. Capacity discharged (C_d) is used in place of SOC, as this eliminates ambiguity in defining and estimating the SOC (cited by [64] as the greatest source of experimental error) and maintain consistency across new and aged cells. Where SOC is given as a reference, it is derived from the capacity discharged. Test points for capacity discharged are evenly spaced based on the measured capacity of the module, with an extra point adjacent to the fully

charged and fully discharged states. Test points for the temperature are chosen to span typical operating temperatures. The test points for both variables are shown in Table 5.1 and the test grid is formed by every combination of the two variables.

Table 5.1: Test points for capacity discharged and temperature used to form the test grid.

Capacity Discharged, C_d [A h]	0, 4.55, 9.1, 18.2, 27.3, 36.4, 45.5, 54.6, 63.7, 72.8, 77.35, 81.9, 86.45, 91
SOC [%] (<i>reference only, derived from capacity discharged</i>)	100, 95, 90, 80, 70, 60, 50, 40, 30, 20, 15, 10, 5, 0
Temperature, T [°C]	40, 20, 0, -20

In order to reduce unnecessary cycling of the cells, the module is exposed to each temperature point before proceeding to the next capacity discharged point. This avoids further opportunity for error and further delays to accommodate voltage relaxation. The test begins with a fully charged (i.e. $C_d = 0$) and fully relaxed battery. For each capacity discharged point, the test procedure is as follows:

1. Discharge to required capacity discharged
 - 1.1. Chamber set to 25 °C
 - 1.2. Close cell cyclers relays
 - 1.3. Close data logger voltage sense relay
 - 1.4. Discharge at 10 A ($\approx C/10$) until desired capacity discharged
 - 1.5. Open all relays (data logger continues periodic voltage measurements)
2. Minimum 8-hour pause for voltage relaxation after discharge

3. Cycle through temperature test points

3.1. 8-hour soak time at 40 °C

3.2. 8-hour soak time at 20 °C

3.3. 8-hour soak time at 0 °C

3.4. 8-hour soak time at -20 °C

4. Repeat steps 1-3 for next capacity discharged point

The environmental chamber setpoint temperatures at each SOC test point are also shown in Figure 5.2.

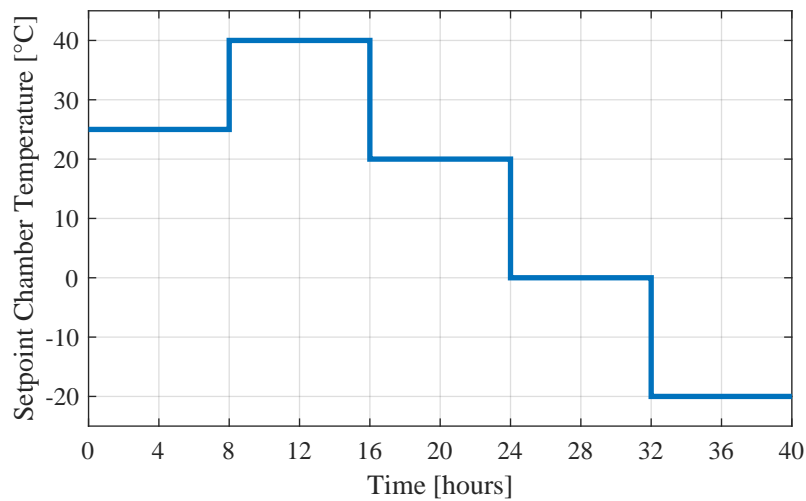


Figure 5.2: Environmental chamber temperature program for each SOC point.

The 8-hour pause for voltage relaxation and the 8-hour soak time at each temperature are determined from an initial test where the rate of change of cell voltage and temperature (respectively) are monitored until they fall to an acceptable level.

Following a charge or discharge, the voltage is considered to be relaxed when the battery has reached a state of electrochemical equilibrium, as indicated by the rate of change of OCV falling below what is significant for the test. Relaxation time is high due to the sensitivity of the voltage measurements, and the soak time is high due to the large thermal mass of the cell module. A relatively low discharge current of 10 A (approximately C/10) is selected in order to reduce the time required for voltage relaxation.

5.2.2 Compensation for Self-Discharge and Voltage Relaxation

Over the duration of the test, the self-discharge and voltage relaxation present a problem similar to the unwanted discharge through sensor leads: they cause measurable decrease in OCV over the test. The self-discharge cannot be avoided and must be corrected following the test, as noted in [29, 64]. At each test point, the rate of change of OCV at steady state is extracted. The steady state rate of change of OCV then forms a lookup table (LUT) which is used to compensate the measurement throughout the test. The OCV compensation is conducted as a cumulative sum:

$$OCV_{corr}(k) = OCV_{meas}(k) - \sum_{N=0}^k \left(\frac{\partial OCV}{\partial t} \right)_k (t_k - t_{k-1}), \quad (5.4)$$

where OCV_{corr} is the corrected OCV, OCV_{meas} is the measured OCV, k is the current time step, $(\partial OCV/\partial t)_k$ is the steady state rate of change of OCV with time at time step k (obtained from the LUT at temperature T and capacity discharged C_d), and

t is the time elapsed. Though the intention is to start the test only once the voltage relaxation rate has fallen below an acceptable threshold, any remaining relaxation will also be corrected under this method. Figure 5.3 shows an example of corrected and uncorrected OCV measurements for $C_d = 9.1 \text{ A h}$ ($\approx 90\%$ SOC).

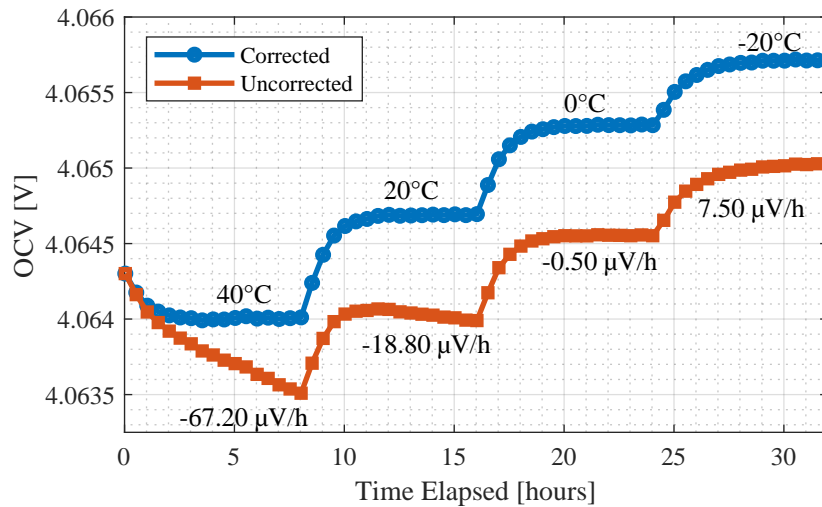


Figure 5.3: OCV vs. Time at $C_d = 9.1 \text{ A h}$ ($\approx 90\%$ SOC), before and after applying the correction for self-discharge rate. By correcting for self-discharge, the OCV measurement becomes constant once thermal equilibrium is reached.

From Figure 5.3, it can be seen that the self-discharge is much more pronounced at the higher temperature points. At lower temperatures, the self-discharge can no longer be observed from this plot.

The self-discharge correction factors across the range of temperatures and SOC tested are shown (as rate of change of open-circuit voltage with time) in Figure 5.4. Following the test procedure, the module is first discharged to the required charge level, then exposed to the range of test temperatures. The data points in this plot are obtained from the voltage measurements at thermal equilibrium, with the

cell cyclers leads disconnected from the module. From this figure, the temperature dependence of self-discharge rate is further demonstrated, as it can be seen that changes to OCV are more pronounced at higher temperatures and appear muted at lower temperatures. It can also be seen that the rate of voltage decrease is much higher at the fully charged state (i.e. $C_d = 0$).

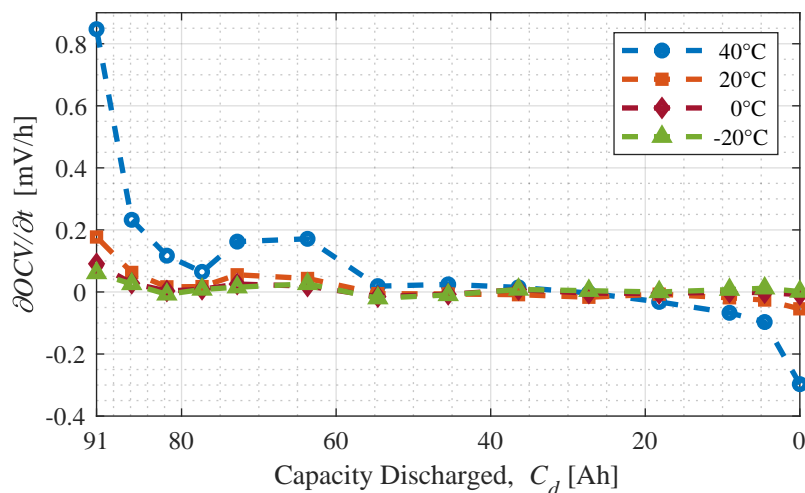


Figure 5.4: Correction factors derived from rate of change of OCV with time ($\partial OCV/\partial t$) at thermal equilibrium.

Figure 5.4 also appears to show an increasing OCV at low SOC (i.e. high C_d), this is likely caused by insufficient relaxation time, which is subsequently captured by the correction factor at these points. This suggests a longer time constant for voltage relaxation at low SOC, where this effect is most pronounced. Since the test begins with the 40°C point at each SOC, a higher rate of relaxation is observed at these points.

5.3 Behavior of the Entropic Heating Coefficient

Depending on the charge level of the cells, they may exhibit either a positive or negative entropic heating coefficient. Examples of both cases are presented in Figures 5.5 and 5.6. In these plots, the ambient temperature is varied according to the test plan and the effect on the OCV is observed. The module is not charged or discharged until the end of the temperature sequence, when the test proceeds to the next test point of capacity discharged.

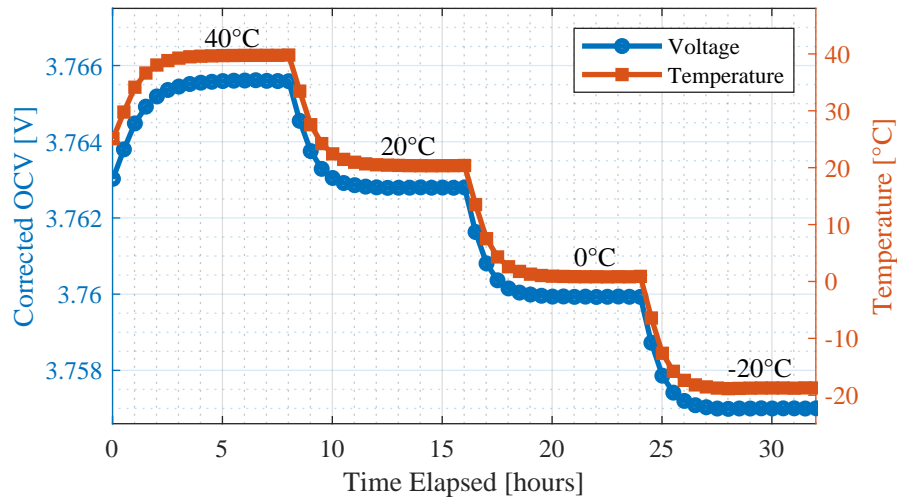


Figure 5.5: Corrected OCV response yielding positive entropic heating coefficient shown at $C_d = 36.4 \text{ A h}$ ($\approx 60\%$ SOC).

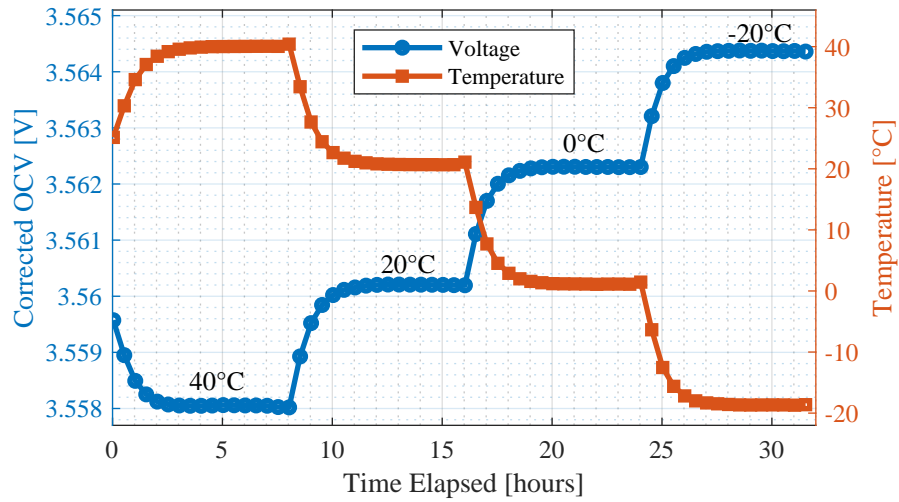


Figure 5.6: Corrected OCV response yielding negative entropic heating coefficient shown at $C_d = 72.8 \text{ A h}$ ($\approx 20\%$ SOC).

5.4 Entropic Heating Coefficient Map

The final results of the entropic heating coefficient test are shown in Figure 5.7.

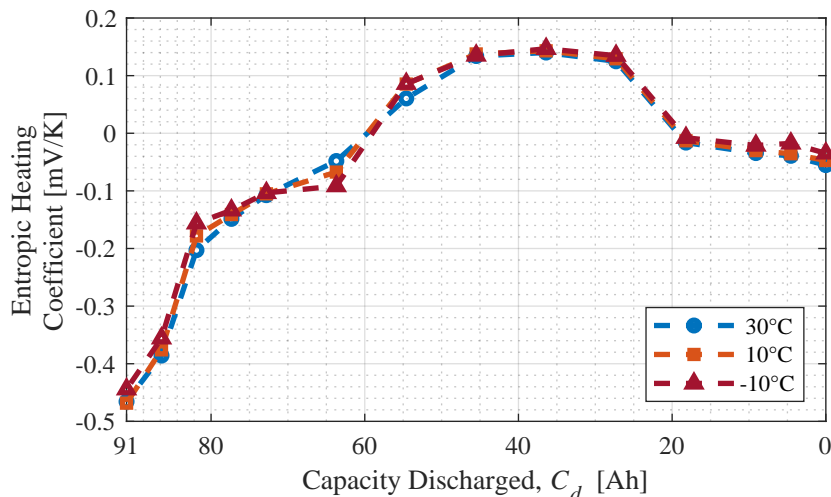


Figure 5.7: Entropic heating coefficient map obtained from testing. It can be seen from this plot that there is no significant temperature dependence observed over the range of temperatures tested.

The magnitudes and behavior of the entropic heating coefficient obtained here are similar to published values for the LFP cell studied in [29]. Existing literature has found the entropy change of NMC cells to be comparable to that of LFP cells [33]. Nevertheless, it remains important to determine the entropic heating coefficient of the specific cell chemistry in order to gain an accurate understanding of the reversible heat generation in the cell.

According to Equation 5.1, charging will lead to an exothermic reaction from the reversible losses in a region of positive entropic heating coefficient, and an endothermic reaction from the reversible losses in a region of negative entropic heating coefficient. Discharging will lead to an endothermic reaction from the reversible losses in a region of positive entropic heating coefficient, and an exothermic reaction from the reversible losses in a region of negative entropic heating coefficient.

It can be seen that the entropic heating coefficient does not show any significant variation with temperature across the test points. The relatively large, negative coefficient at low charge (i.e. high C_d) indicates a strong endothermic reaction from the cells when charging from a depleted state, or a large exothermic reaction when discharging at low SOC.

Without compensation for self-discharge and voltage relaxation, the entropic heating coefficient map shows more scatter across temperatures at low charge, as shown in Figure 5.8, this is very similar to the map presented in [29].

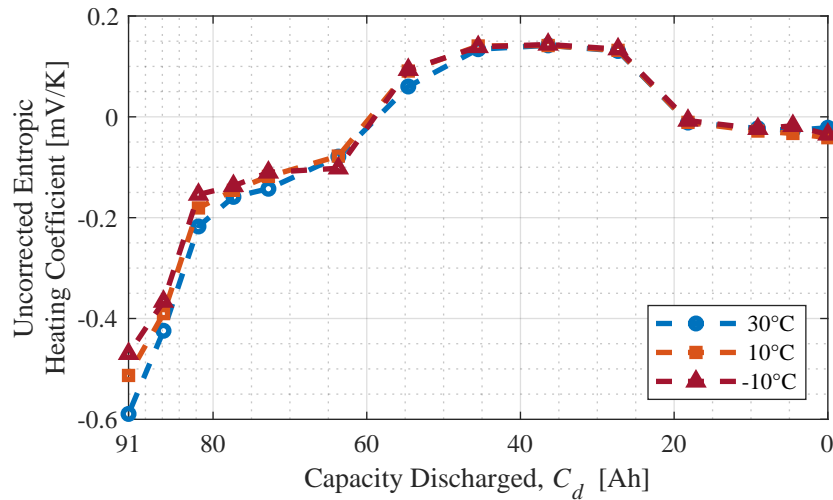


Figure 5.8: Entropic heating coefficient map obtained without compensation for self-discharge and voltage relaxation, showing more scatter at low charge.

5.5 Loss Modelling with Entropic Heating Coefficient

Once the entropic heating coefficient is determined, the cell losses are modelled using Equations 5.1 through 5.3. Other inputs to the model (i.e. current, temperature, open-circuit voltage, and terminal voltage) are obtained either by measurement or through the use of other modelling techniques, such as an equivalent circuit model (ECM) [65]. *For previously characterized cells, an ECM enables the modelling of any arbitrary cycle without the need for further laboratory testing.* Here, for the purpose of comparison, the inputs for the cell loss model are obtained from measured data. Open-circuit voltage is obtained as a function of capacity discharged using measurements from an HPPC test, as outlined in [53], and accessed using a LUT for the purposes of the cell loss model. The entropic heating coefficient is obtained from the map using a LUT for temperature and capacity discharged. Linear interpolation is used in conjunction with the LUTs.

Unless another temperature is indicated, measured data is obtained using the active cooling module with a constant supply of 20 °C coolant and the environmental chamber maintaining a 20 °C ambient temperature. For reference, a constant resistance approximation to the cell loss is calculated using the round-trip (charge-neutral charge and discharge) energy loss obtained from cell cyclers measurements. This is obtained by distributing the energy loss measurement proportionally according to the measured current squared. Using Equations 5.1 through 5.3, cell losses are predicted for 1C, 3C, and 5C charges and presented in Figures 5.9 through 5.11. *Note*

the different limits of both axes across the three plots.

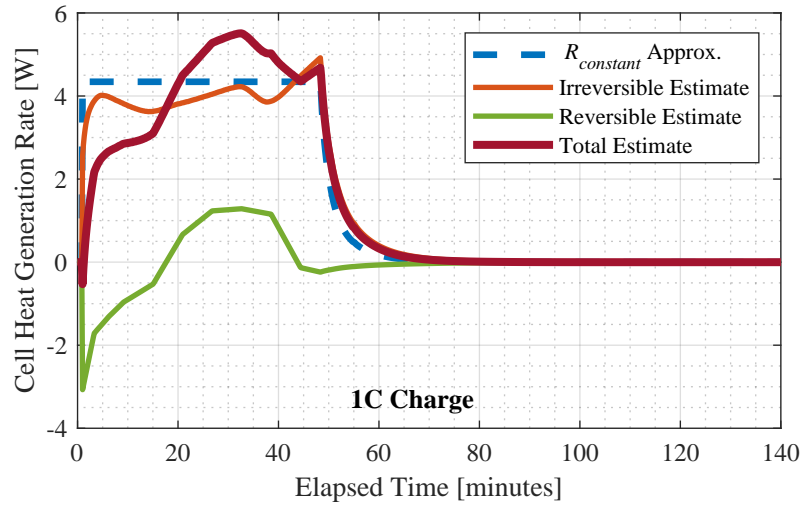


Figure 5.9: Modelled cell losses for a 1C charge.

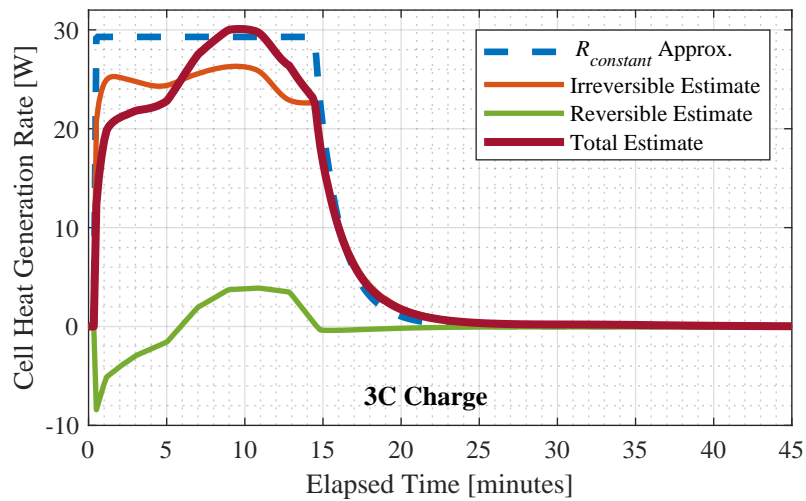


Figure 5.10: Modelled cell losses for a 3C charge.

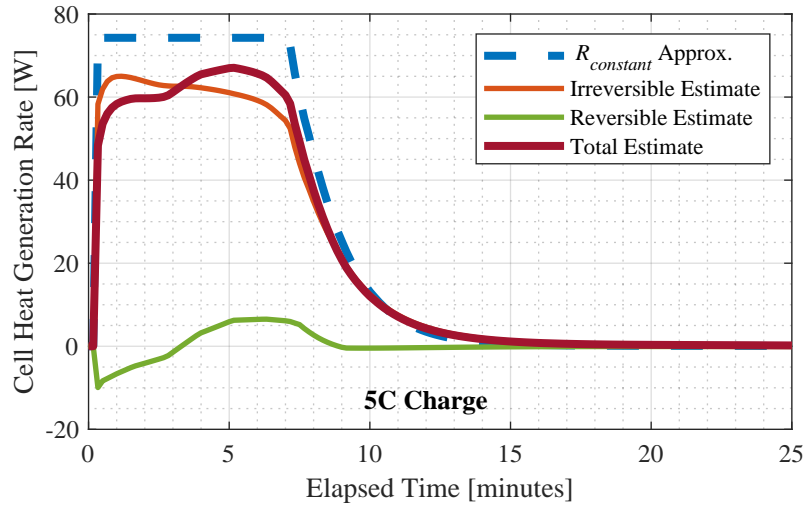


Figure 5.11: Modelled cell losses for a 5C charge.

Figures 5.9 through 5.11 illustrate the importance of considering the reversible heating contributions, especially at low charge rates. As the charge rate increases, the contribution of the reversible losses to the total losses decreases. This can be explained by comparing Equation 5.1, which shows the reversible losses growing with the current, with Equation 5.2, which shows the irreversible losses growing with the squared current. Nevertheless, it is evident that the reversible losses play an important role and should not be overlooked, even at higher charge rates.

5.5.1 Reversible Heating Contribution

Figure 5.12 further illustrates the significance of the reversible heat at low charge rates, and the diminishing contribution as charge rate increases.

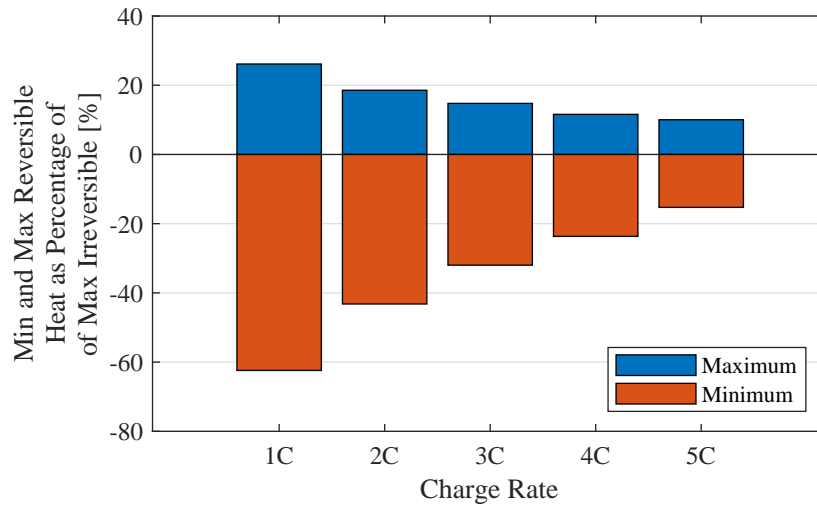


Figure 5.12: Maximum and minimum reversible heat generation rate as a percentage of maximum irreversible heat generation rate.

The strong endothermic response when charging at low SOC is also apparent in this figure, as the maximum endothermic response of the reversible heat reaches over 60% of the maximum irreversible heat for the 1C charge. This is due to the large, negative values of entropic heating coefficient observable in Figure 5.7. As shown in Figures 5.9 through 5.11, the endothermic response quickly disappears as the battery is charged, due to the steep slope of the entropic heating coefficient at low SOC.

5.5.2 Temperature Contribution

Peak cell loss for a series of 4C charges at different temperatures are presented in Figure 5.13. For these tests, the temperatures of the liquid coolant and environmental chamber are fixed to the indicated values.

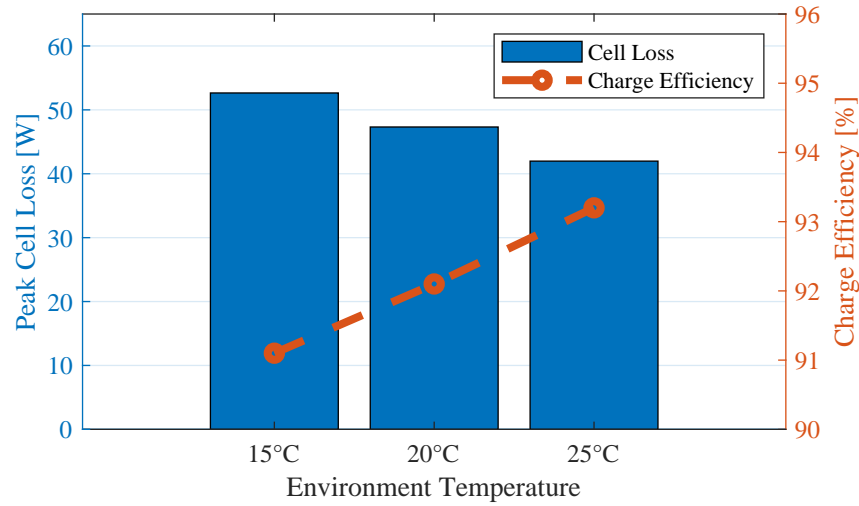


Figure 5.13: Peak cell loss for a series of 4C charges at different temperatures.

As shown in Figure 5.13, these loss estimates lead to charging efficiencies of 91.1% for the 15 °C charge, 92.1% for the 20 °C charge, and 93.2% for the 25 °C charge. At the pack level, this leads to savings of more than 7 kW under extreme fast charge rates, which leads to further savings in the form of reduced thermal management loads. Since the entropic heating coefficient does not vary significantly with temperature and the temperature change between the three cases is small on an absolute scale, it can be seen from Equations 5.1 and 5.2 that the driving force behind the reduction in peak cell loss is the irreversible losses. This irreversible loss characteristic is due to the cell resistance being significantly higher at lower temperatures, which is common for Li-ion cells.

5.5.3 Peak Loss Comparison

Figure 5.14 shows peak cell loss for all tested charge rates at 20 °C.

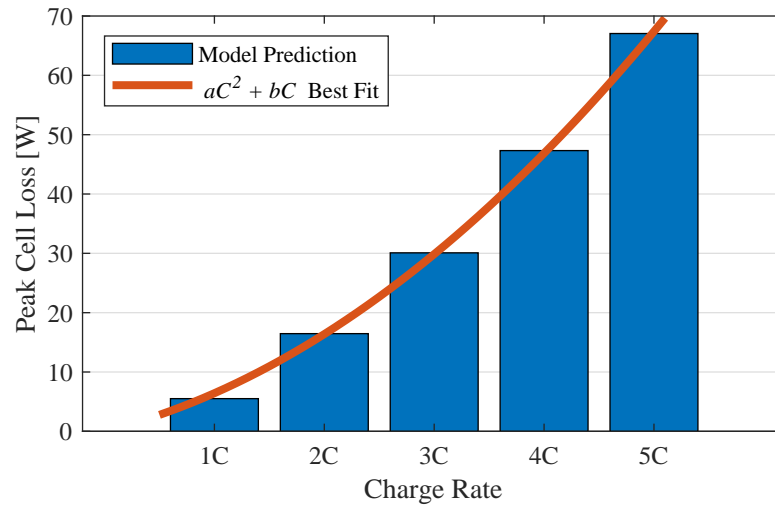


Figure 5.14: Peak cell loss shown for a series of 20 °C charges from 1C to 5C.

As the nature of Joule heating is to vary with the square of the current, the sharp increase in peak cell loss with charge current is consistent with expectations. Since the reversible heat generation represents a greater proportion of the total heat generation at lower charge rates, increases in heat generation cannot be predicted by considering the squared current alone. Alongside the model prediction, Figure 5.14 shows the peak cell loss from an $aC^2 + bC$ best fit line (where C is the charging C-rate and a and b are constants with values of 1.8 W C^{-2} and 4.7 W C^{-1}), showing good agreement with the cell loss model prediction.

Chapter 6

Module Thermal Modelling

Thermal models are developed for the module presented in Chapter 4. These models are developed using two different methods: computational fluid dynamics and recurrent neural networks.

Under the first approach, knowledge and assumptions of the underlying physics are used to determine a set of governing equations to be solved numerically. This CFD-based method requires an understanding of the governing equations, dominant physical reactions, and material properties of the cells and module components, as well as an estimate of the internal heat generation of the cells. Under the second approach, cell temperatures are predicted using recurrent neural networks. Instead of a physics-based approach, temperatures are predicted using previously obtained testing data by selecting relevant input parameters.

These models are used to predict cell temperatures for a series of charge rates up to 5C. The CFD model is also used to predict temperatures over a combined cycle

of driving and periodic fast charging.

6.1 CFD-based

ANSYS Fluent is first used to model the coolant flow thermal behaviour in the module at steady state. From the steady state model, the heat transfer coefficient from the pipe wall to the coolant, and the temperature rise of the coolant are determined. Transient, thermal-only modelling is conducted in ANSYS Mechanical using knowledge of these parameters obtained from the thermal-fluid model—eliminating the need for fluid flow modelling within the transient simulations. This greatly reduces the computational cost of the transient simulations since much of this cost comes from the more fine mesh and the extra governing equations required to resolve the fluid flow. Both CFD models employ the heat generation model developed in Chapter 5 to determine the internal heat generation of the cells. Rounded edges of the cold plate are represented as right angles in order to improve meshing.

Existing literature has shown the impact of current density on temperature distribution [7,9]. Though it is possible to apply the loss model presented in Chapter 5 to a spatially-varying current density, for simplicity, both the thermal-fluid model and the thermal-only model approximate the internal heat generation as being uniform throughout the volume of the cells. This approximation which neglects the variation in current density within the cells.

6.1.1 Detailed Steady State Thermal-Fluid Model

ANSYS Fluent is used to model the flow of coolant and the thermal behaviour of the battery module at steady state. This model is employed to solve the energy equation with a constant source term, the conservation equation, the three momentum equations for a three-dimensional viscous flow, and the two equations of the selected turbulence model. This more detailed model allows for the convection coefficient and temperature rise of the cooling fluid to be determined. Due to the additional equations and meshing requirements needed to simulate the fluid flow inside the copper pipe of the cold plate, this model is computationally costly and therefore not well suited for transient simulations. A symmetry boundary condition is used to reduce the model to only half the width of the module; symmetry cannot be applied to reduce the height of the module due to the flow of coolant through the u-shaped bend of the copper pipe. This model is shown in Figure 6.1.

From the results of the steady state analysis, the convection coefficient of the coolant inside the copper pipe is calculated as:

$$h_{coolant} = \frac{q''}{T_{surf} - T_{bulk}}, \quad (6.1)$$

where q'' is the heat flux through the interface of the coolant and the copper pipe, T_{surf} is the area-weighted average surface temperature of the copper pipe at this interface, and T_{bulk} is the mass-weighted average temperature of the coolant. These variables are obtained as parameters directly from ANSYS Fluent.

The only energy source in the model is the internal heat generation of the battery

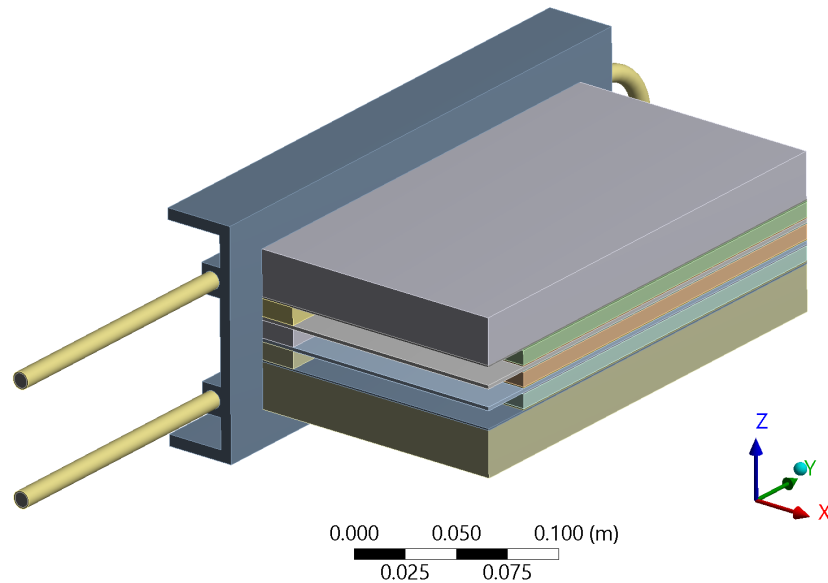


Figure 6.1: Geometry of thermal-fluid model, with a symmetry plane used to reduce the width of the model (x -direction).

cells and the only energy sink is the flowing coolant. The Reynolds number—based on the inner diameter of the copper pipe in the cold plates, a volumetric flow rate of 15 L min^{-1} , and the fluid properties listed in Table 4.3—is 4570. The governing equations are solved iteratively until the absolute residuals of all governing equations fall below 10^{-6} .

Choice of Turbulence Model

The Reynolds number of the coolant flow suggests a transitional or turbulent flow in the free-stream, and the u-shaped bend in the copper pipe may lead to separation or dean vortices. The SST $k-\omega$ turbulence model [66] is used to capture these effects in the bend, and to model the coolant flow in the sections of straight pipe.

Mesh Independence Study

A conformal, Cartesian mesh is used at the interfaces, including a Cartesian mesh at the interface between the cold plate and the bars, plastic, and inter-cell plates.

Here, the calculated convection coefficient from Equation 6.1 is used to monitor mesh sensitivity. This captures any changes in the heat flux through the pipe, in the pipe surface temperature, or in the mean coolant temperature. Results of the mesh independence study are presented in Table 6.1.

Table 6.1: Calculated convection coefficient for different meshes, and percentage difference compared to mesh A3.

Mesh	A1	A2	A3
Number of elements	1 115 314	2 749 864	6 505 167
Convection coefficient [$\text{W m}^{-2} \text{K}^{-1}$]	4518 (+10%)	4179 (+1.7%)	4108 (baseline)

Since the steady state model must only be solved once to determine the heat transfer coefficient, the most fine mesh (A3) can be used without increasing the computational cost of subsequent calculations. Mesh A1 is shown in Figure 6.2.

Calculated Convection Coefficient

From the numerical results, and according to Equation 6.1, the convection coefficient of the coolant flow inside the copper pipe is calculated as $4108 \text{ W m}^{-2} \text{ K}^{-1}$ for the most fine mesh, as shown in Table 6.1. For the straight-pipe section, the Gnielinski correlation [67] predicts a convection coefficient of $3476 \text{ W m}^{-2} \text{ K}^{-1}$; the u-shaped bend is expected to enhance the straight-pipe convection, which is consistent with the numerical model results.

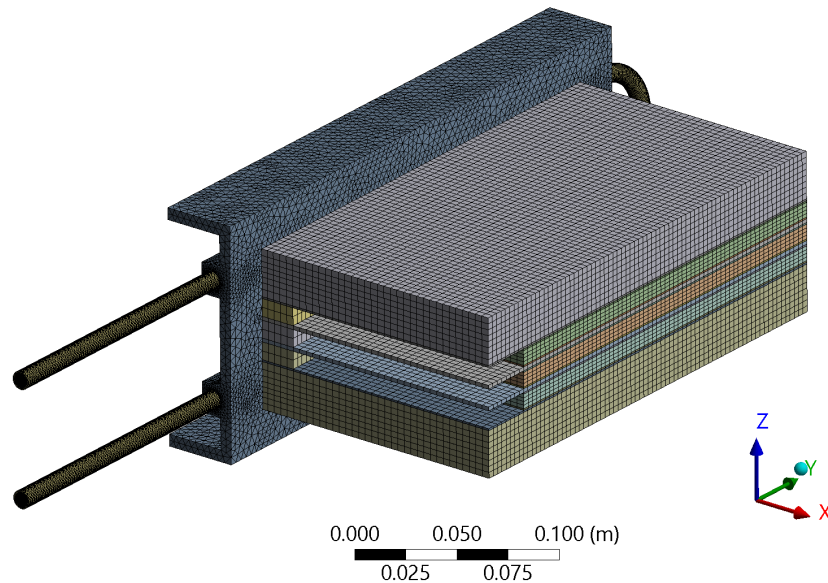


Figure 6.2: Mesh of detailed, steady state thermal-fluid model, used to determine convection coefficient of coolant.

6.1.2 Thermal-Only Transient Model

Transient, thermal-only modelling is accomplished using the Transient Thermal feature within ANSYS Mechanical. The thermal-only model is used to solve the energy equation with a time-varying source term in order to simulate the series of fast charges. The results of these simulations are then compared to the experimental measurements. The coolant is fixed at its bulk mean temperature determined in the coolant flow simulation, and the convection coefficient is configured to be consistent with Equation 6.1. All exterior surfaces are configured as convection boundaries to represent convection to the surrounding air in the environmental chamber. Since the coolant flow is no longer included in the model, an additional symmetry plane may be used, and the model must only represent half of the module thickness and half of

the height, as shown in Figure 6.3.

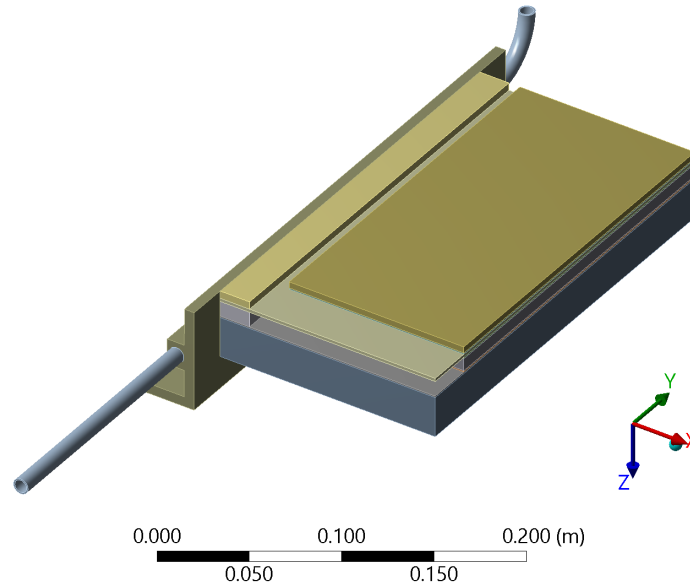


Figure 6.3: Geometry of thermal-only model, with symmetry planes used to reduce the width (x -direction) and height (z -direction) of the model.

Mesh Sensitivity Study

A mesh independence study is conducted for the thermal-only model. Three different meshes are generated, with 11 910, 18 030, and 23 907 elements. The modelled peak temperature during the 5C charge is used to compare the solution across the different meshes.

Table 6.2: Peak temperature during 5C charge for different meshes, and percentage difference in temperature *rise* compared to mesh B3.

Mesh	B1	B2	B3
Number of elements	11 910	18 030	23 907
5C Charge Peak Temperature [$^{\circ}\text{C}$]	34.053 (-1.1%)	34.212 (0%)	34.212 (baseline)

Mesh B1, the most coarse mesh, shows a temperature *rise* deviation of only 1.1% from the most fine mesh. In order to minimize computational cost, mesh B1 is used for the remainder of this work. This mesh is shown in Figure 6.4.

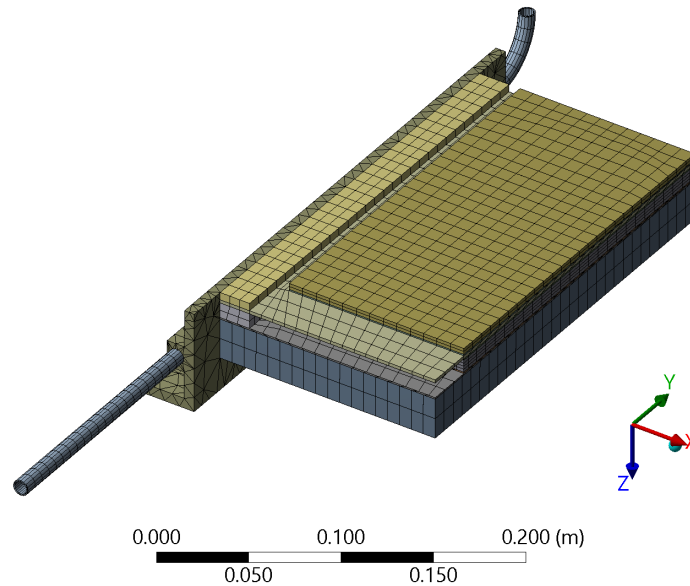


Figure 6.4: Mesh of thermal-only model, used to determine module temperatures during transient simulations.

As with the more detailed, thermal-fluid model, conformal mesh is used at the interfaces, including a Cartesian mesh at the interface between the cold plate and the bars, plastic, and inter-cell plates.

6.2 Neural Network-Based

The numerical, physics-based modelling techniques presented in Section 6.1 rely on a thorough understanding of the governing equations, dominant physical reactions, and material properties—not only of the battery cells and module components, but

also of the thermal management system and coolant flow. These thermal models are also costly to develop and costly to execute, both initially and on subsequent calculations. Here, recurrent neural networks are investigated as an alternative to these numerical solutions. It must be stressed that the use of RNNs for predicting module temperatures is only possible in the presence of existing, module-specific, laboratory testing data. Once a neural network has been trained, subsequent calculations are very computationally inexpensive. This means that NNs may be deployed for online temperature estimation, on-board an EV, without requiring significant computational resources.

This section is not intended to be an exhaustive study on the use of neural networks for battery thermal modelling, but rather as an initial investigation and a means for comparison with the numerical modelling techniques presented.

6.2.1 Architecture and Training

A long short-term memory (LSTM), recurrent neural network is selected for this application. LSTM networks include outputs of past time steps as a parameter to aid in the prediction of future time steps [68]. This is useful in the estimation of temperature during fast charging, as the transient nature of the problem means that the temperature at future time steps is a function of the temperature at past time steps. This better represents the effect of the thermal mass.

For this application, the input parameters are the instantaneous current (I), terminal voltage (V_T), and remaining battery capacity (C). The RNNs uses these inputs to predict the maximum temperature (T_{max}) and maximum temperature *difference*

(ΔT_{max}) at each time step, based on measurements recorded at the five locations on the surface of the middle cell shown in Figure 4.2a. Data recorded from the test module are used to train the networks; charging data are available at rates from 1C to 5C, in 1C increments. The RNNs are composed of an input layer, an LSTM layer, two fully connected layers, and an output layer. They are constructed in MATLAB R2018b using the Deep Learning Toolbox [69]. The network architecture is shown in Figure 6.5, where the subscript k denotes the time step.

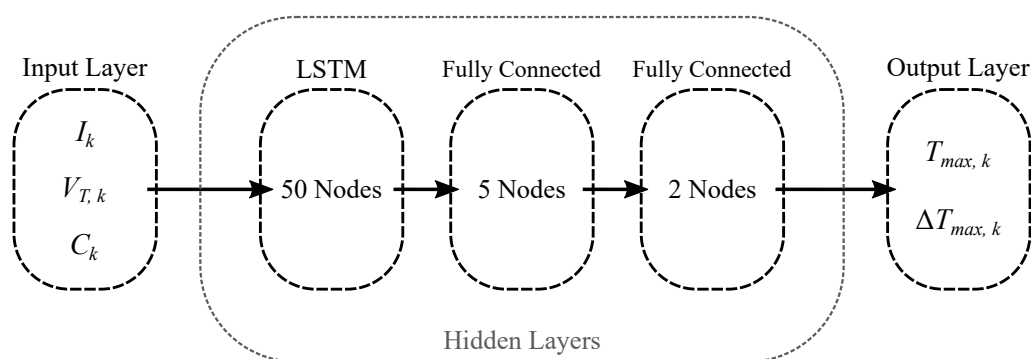


Figure 6.5: Architecture of the recurrent neural networks .

Three separate LSTM RNNs are created—all based on this architecture—to investigate the ability of the RNN to predict module temperatures. The first network is trained using 1C, 3C, and 5C charging data and validated using the 2C and 4C charging data. The purpose of this network is to test the interpolative capabilities of LSTM neural networks (i.e. ability to predict when operating inside training data power limits). The remaining networks are intended to test the extrapolative capability of the RNN (i.e. ability to predict when operating outside training data power limits). One is trained using 2C, 3C, and 4C charging data and validated using the 1C and 5C charging data (bilateral extrapolation); the other is trained using 1C, 2C,

and 3C charging data and validated using the 4C and 5C charging data (unilateral extrapolation). The purpose of the third network is to further test the extrapolative capabilities of LSTM neural networks beyond the training data and to investigate the ability to predict the thermal response characteristics observed at higher C-rates.

Each network is trained for up to 5000 epochs using a decreasing learning rate. After a reasonable root-mean-square-error (RMSE) is obtained, each network is reset to a higher learning rate and training is continued. The purpose of resetting the learning rate is to reduce the likelihood of convergence on local minima. The MATLAB Training Progress window for the interpolative network training is presented in Figure 6.6.

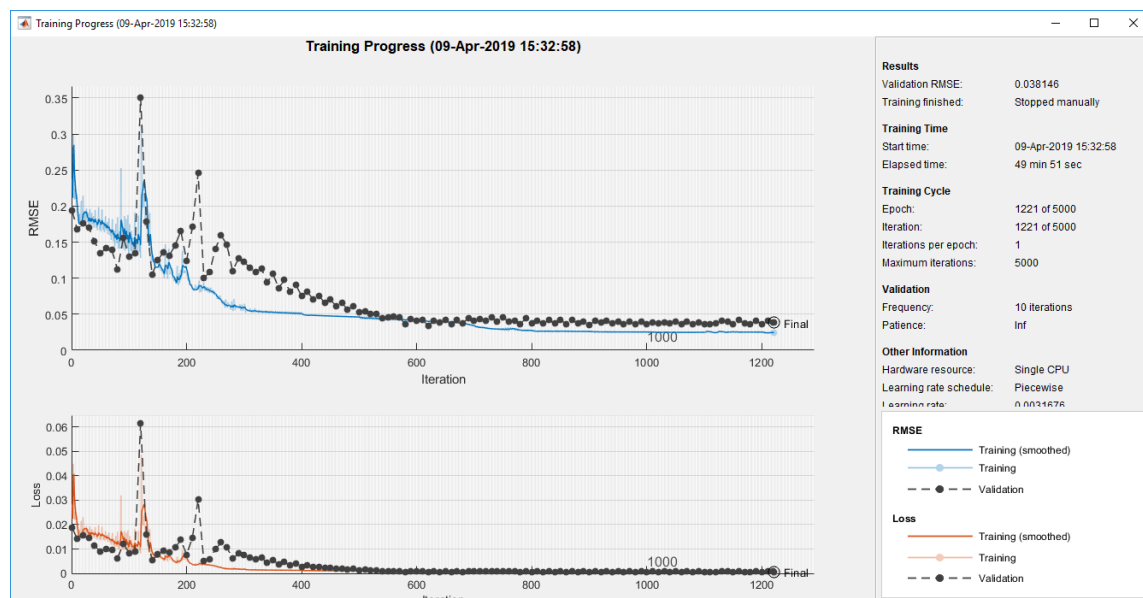


Figure 6.6: MATLAB Training Progress window, showing training of interpolative network.

The results of each network are compared to measurements obtained from the test

module described above, and the error between the prediction and measurement is calculated. This provides insight into the capabilities and limitations of temperature prediction using LSTM neural networks.

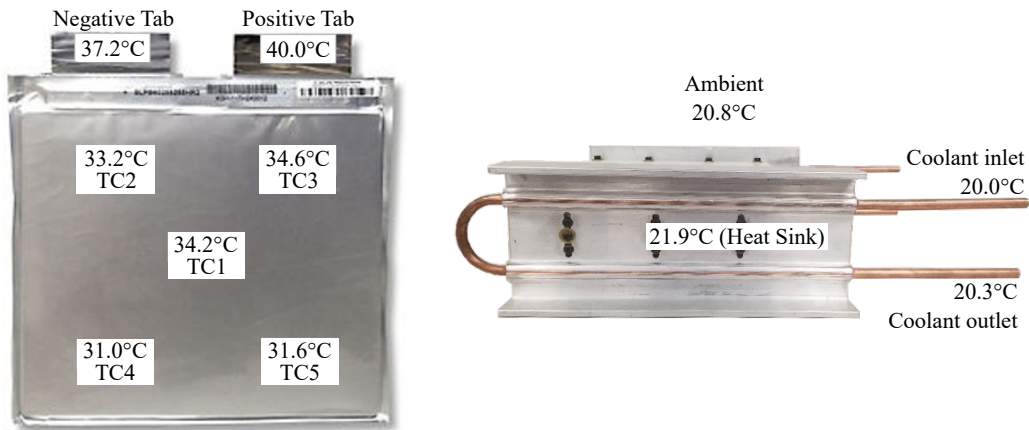
Chapter 7

Module Experimental

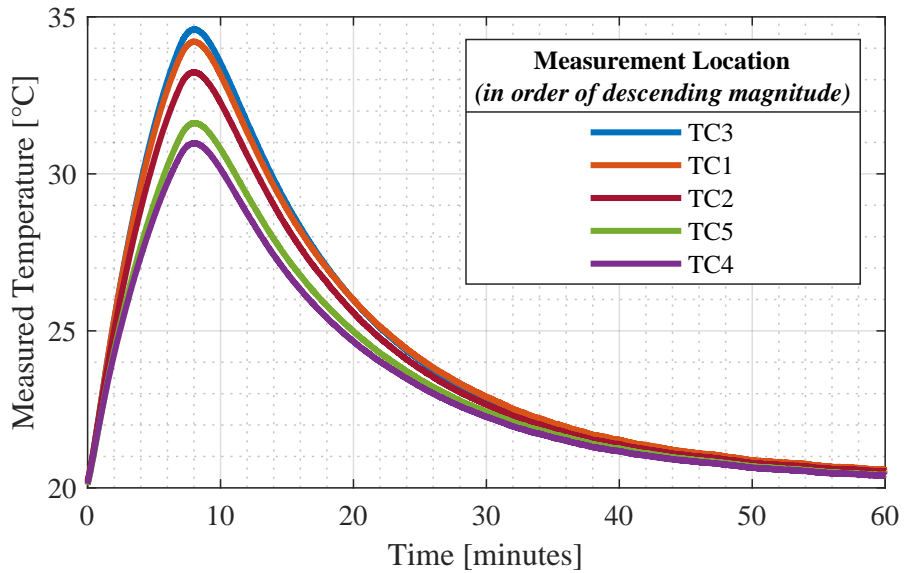
Measurements and Validation of

Thermal Modelling

Experimental measurements for the inter-cell cooling module are obtained using the test setup described in Section 3.2. Charging is conducted using the CC-CV protocol. Where a C-rate is provided, it defines the current magnitude during the constant current portion of the charge, after which the current drops sharply to maintain a constant terminal voltage. Figure 7.1a shows the peak temperature measurements of the cell and module during the 5C charge; measured temperatures on the cell face throughout the charge are shown in Figure 7.1b.



(a) Peak temperature measurements for a 5C charge.



(b) Cell face temperature measurements for 5C charge.

Figure 7.1: Cell and module temperature measurements for a 5C charge.

Figure 7.1 also shows the impact of the non-homogeneous current density inside the battery cell, with the temperature increasing toward the positive tab. This is not captured in the numerical model, which assumes a uniform heat generation and

a uniform current density.

For the CC-CV charges conducted, the measured peak temperatures occur at the transition from constant-current to constant-voltage. Figures 7.2 and 7.3 show measured temperature and current magnitude (shown as C-rate), over a 5C charge and a 3C charge, respectively. These plots show the relationship between temperature rate and current magnitude.

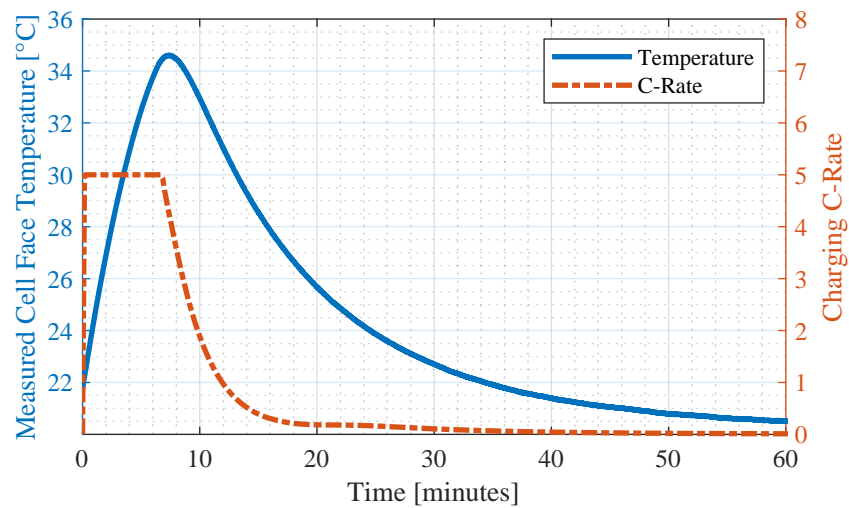


Figure 7.2: Measured tab-adjacent cell face temperature and current magnitude (shown in C-rate) for a 5C charge. Measurement corresponds to location TC3 as indicated in Figure 7.1a.

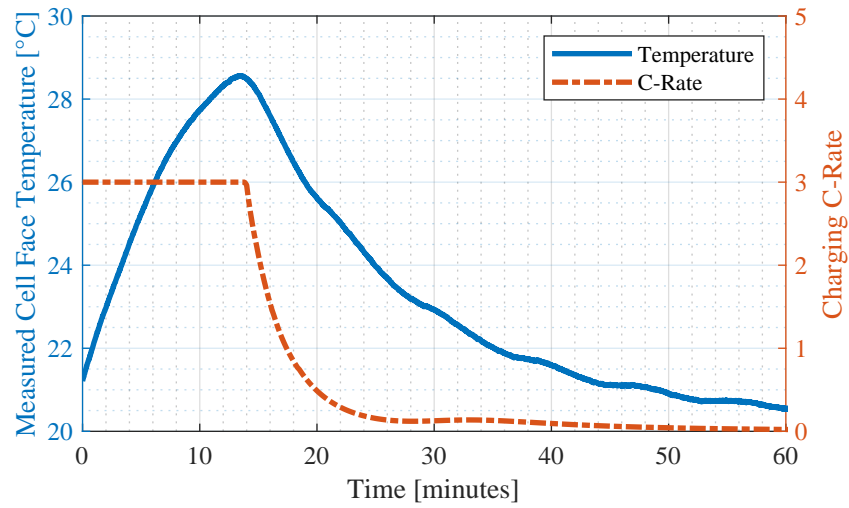


Figure 7.3: Measured tab-adjacent cell face temperature and current magnitude (shown in C-rate) for a 3C charge. Measurement corresponds to location TC3 as indicated in Figure 7.1a.

7.1 Steady State

7.1.1 Measured and CFD-Modelled Temperature for Constant Loss

A current signal following a zero-offset square wave is used to generate a constant loss in the battery module without a net charge or discharge to the cells. Module currents are selected to correspond C-rates ranging from 1.5C to 3.5C, in increments of 0.5C. Steady state temperatures corresponding to the constant loss values are presented in Table 7.1.

Table 7.1: Temperature prediction error at steady state. Percentage error is calculated using respective cell value as baseline. Modelled temperature corresponds to locations TC2 and TC3, measured cell corresponds to TC3, as indicated in Figure 7.1a.

C-Rate	Module Loss [W]	Modelled Cell Temperature Rise [°C]	Measured Cell Temperature Rise [°C]	Measured Pos. Tab Temperature Rise [°C]
1.5	30.5	3.2	2.1 (52% error)	2.8 (14% error)
2.0	47.4	5.0	3.2 (56% error)	4.5 (11% error)
2.5	74.6	7.8	4.9 (59% error)	6.9 (13% error)
3.0	105.8	11.1	6.8 (63% error)	9.7 (14% error)
3.5	140	14.6	9.0 (62% error)	13.1 (11% error)

Modelled maximum temperatures at steady state are significantly higher than measured values. It is expected that this is due to discrepancy in the thermal conductivity values of the cells used by the model (which are obtained by scaling from known values for a similar cell). If the thermal conductivity values presented in Section 3.4.1 are below their actual values, the ability of the cells to reject heat is impeded in the model, and the steady state temperature would be over-estimated.

This discrepancy may also be due to the fact that heat rejection through the cell tabs is neglected in this model. With all cell cyler channels connected in parallel to the terminals of the module, the power leads may act as extended surfaces through which heat transfer to the environmental chamber may be greatly enhanced. This is not represented in the numerical model.

7.2 Transient

7.2.1 CFD-Based

Measured and Modelled Temperatures for 1C to 5C Charge Rates

For a series of 1C to 5C charges, the measured temperatures are compared to those obtained from the numerical model, and serve as validation for the model. For the 1C, 3C, and 5C charges, measured and modelled temperatures are presented in Figure 7.4.

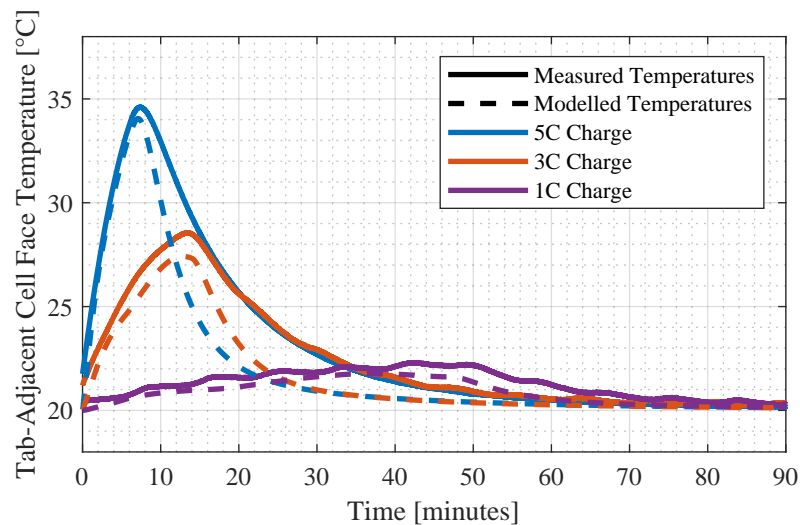


Figure 7.4: Measured peak cell surface temperature for a series of charge rates. Tab-adjacent temperature represents location TC3 for measured data and both TC2 and TC3 for modelled data, as indicated in Figure 7.1a.

For the 5C charge and the 1C charge, the numerical model predicts a peak temperature 0.55°C lower than the measurement. For the 3C charge, the numerical model under-predicts the peak temperature by 1.15°C. It should be noted here that

the temperature *measurement* is accurate only to $\pm 0.7^\circ\text{C}$. The pattern of oscillating measured temperature visible in the 1C charge is caused by throttling of the chiller, since the lower thermal load does not require the compressor to be operated continuously.

Even for the 3C charge, which produces the greatest modelling error, the peak temperature is estimated to within 1.15°C . Recalling that the initial temperature of the fast charge is 20°C and that the measured peak temperature is 28.6°C , this means that the model is able to predict the peak temperature *rise* of the 3C charge to within 14%. For the 5C charge, the peak temperature rise is modelled to within 4%.

Impact of Model Specific Heat Capacity over 5C Charge

To investigate the impact of the cell's specific heat capacity on the modelled cell face temperature, two additional scenarios are presented: a 25% increase in specific heat and a 100% increase in specific heat. For a 5C charge, the impact of these modifications on the modelled temperature is shown in Figure 7.5.

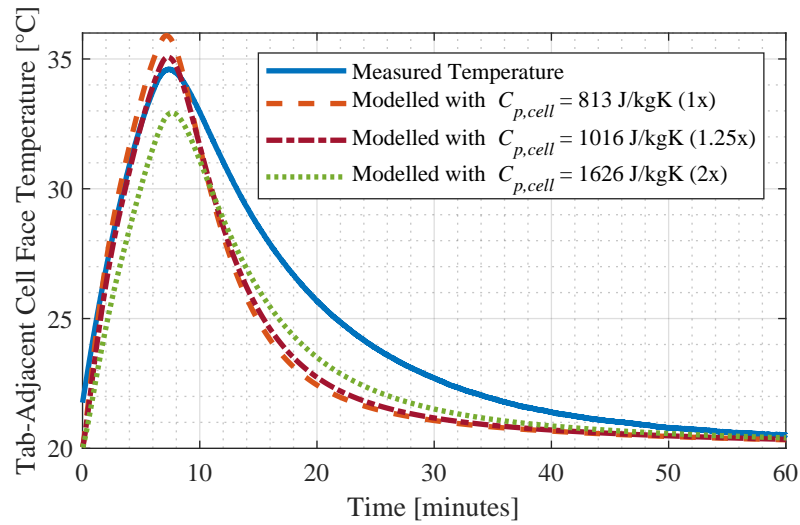


Figure 7.5: Measured and modelled cell face temperature for varying cell specific heat ($C_{p,cell}$). Tab-adjacent temperature represents location TC3 for measured data and both TC2 and TC3 for modelled data, as indicated in Figure 7.1a.

Following the constant current portion of the charge, there is no significant change in temperature for the 25% increase case. A more substantial increase to the cell specific heat is required to see an impact at this stage; a significant difference can be seen when increasing the specific heat by 100%, as shown in the plot. The impact on *peak* temperature, however, appears to be more sensitive to the specific heat capacity; a significant reduction in peak temperature, 0.8 °C, is obtained with an increase of only 25% to the cell specific heat. This shows that an accurate understanding of thermal properties is an important prerequisite to a numerical model.

Measured and Modelled Temperatures for a Series of Repeated Drive Cycles and Fast Charges

A series of repeated drive cycles and fast charges is also studied. Using a vehicle model representing a 2018 Nissan Leaf, battery current and power for a 40 kWh, 4p87s pack are scaled to the 3p1s Kokam Module. Here, the heat generation inside the cells is modelled using an electrothermal model [22]; this approach requires further characterization of the cells, however it removes the approximation of constant internal resistance of the battery cells, adding consideration for current level, terminal voltage, and SOC. For previously characterized cells, the heat generation for an arbitrary drive cycle or charge may be modelled using an equivalent circuit model [65]. Figure 7.6 shows several US06 drive cycles, repeated until depletion of the battery pack, followed by a sustained 4C fast charge for 15 minutes, and then repeated twice more. The driving portion occurring between charges gives sufficient time to remove the excess heat accumulated in the cells during fast charging, as shown in Figure 7.7.

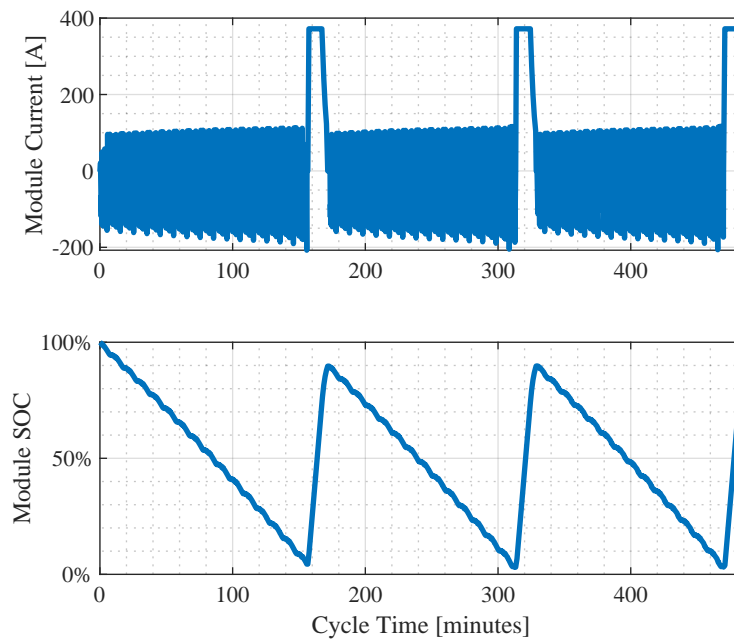


Figure 7.6: Battery module current and SOC for repeated US06 drive cycles and 4C fast charges.

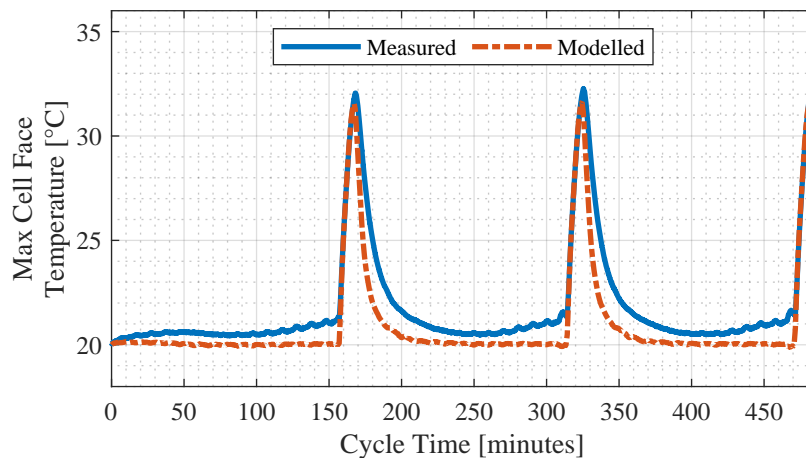


Figure 7.7: Measured and modelled temperatures for repeated US06 drive cycles and 4C fast charges. Maximum temperature on cell face shown.

Here, the peak temperature during the 4C charges is measured to be 32.3 °C, while the model predicts a value of 31.6 °C. This corresponds to an error of 0.7 °C, or 2%. This type of modelling is useful for assessing the performance of a certain battery pack design and studying the impact of design modifications.

7.2.2 Neural Network-Based

Interpolation

The interpolative network is used to predict 2C and 4C charging temperatures using 1C, 3C, and 5C charging training data. The network achieves an RMSE of 0.0381 following training over 1221 epochs. The temperature predictions show a strong level of agreement with the laboratory measurements. Figure 7.8 shows the predicted maximum temperature and the measured maximum temperature obtained from the test module.

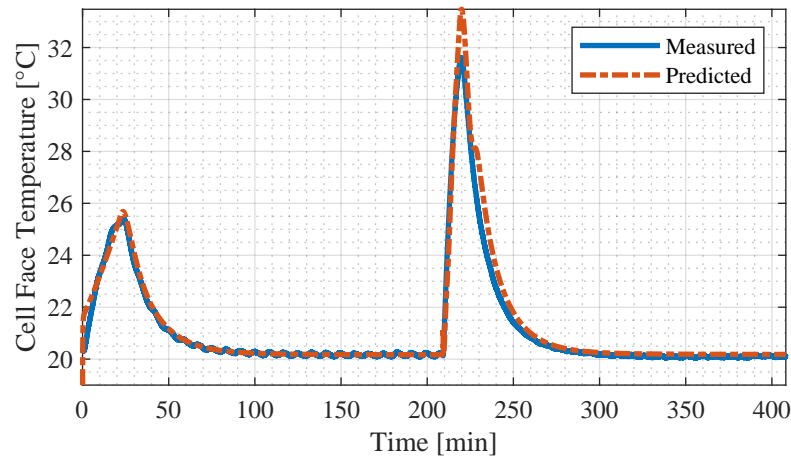


Figure 7.8: Interpolative network predicted maximum cell temperature compared to measured values for 2C and 4C charges (validation set).

As shown in Figure 7.8, the prediction closely follows the measurement during the 2C charge, and accurately models the peak temperature. During the 4C charge, the network is able to predict the temperature profile before and after the peak, though it over-predicts the maximum temperature peak by 1.9°C , equivalent to an over-prediction of temperature *rise* of 16%. Maximum temperature *difference* predictions are presented in Figure 7.9.

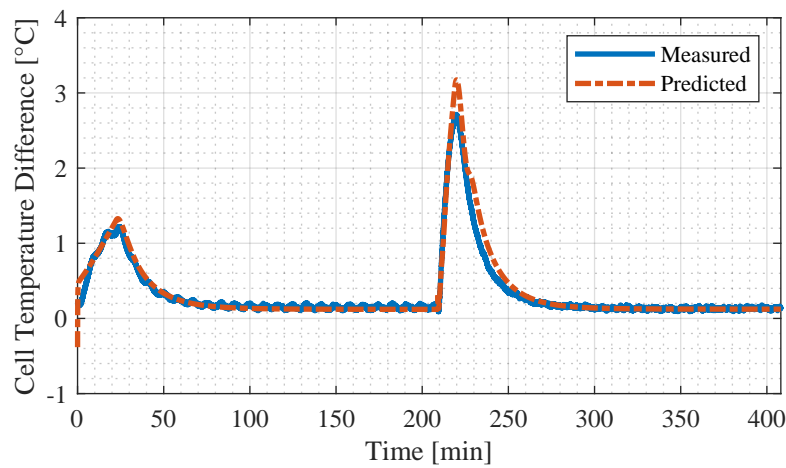


Figure 7.9: Interpolative network predicted maximum cell temperature *difference* compared to measured values for 2C and 4C charges (validation set).

The predicted maximum temperature difference shows similar characteristics to the maximum temperature predictions presented in Figure 7.8. The network is accurate throughout the 2C charge, but over-predicts the peak temperature difference across the cell during the 4C charge by 0.46°C .

Bilateral Extrapolation

The bilateral extrapolation network is used to predict 1C and 5C charging temperatures using 2C, 3C, and 4C training data. The network finishes training after 3328 epochs with an RMSE of 0.0542. Figures 7.10 and 7.11 show the predicted and measured maximum temperature and maximum temperature *difference*.

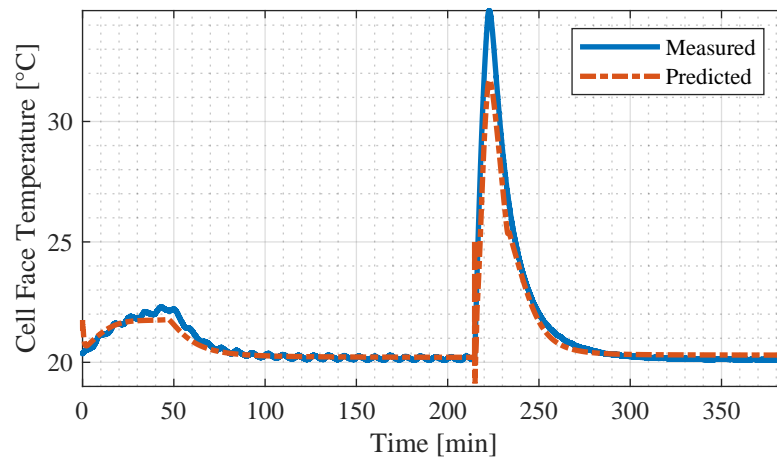


Figure 7.10: Bilateral extrapolation network predicted maximum cell temperature compared to measured values for 1C and 5C charges (validation set).

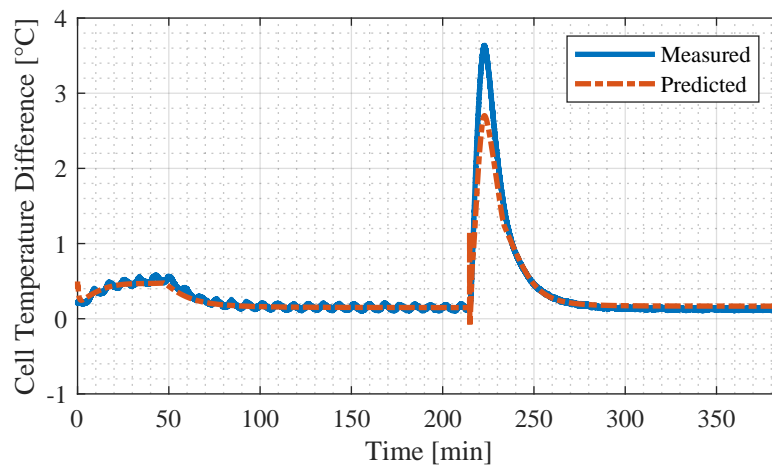


Figure 7.11: Bilateral extrapolation network predicted maximum cell temperature *difference* compared to measured values for 1C and 5C charges (validation set).

Though the bilateral extrapolation network is able to perform fairly well just outside the window of the training data, the results show that this network is not as accurate as the interpolative network. The bilateral extrapolation network is able to accurately predict both outputs during the 1C charge. During the 5C charge, however, the maximum temperature is under-predicted by 2.9°C, equivalent to an under-prediction of temperature *rise* of 20%.

Unilateral Extrapolation

The unilateral extrapolation network is used to predict 4C and 5C charging temperatures using 1C, 2C, and 3C charging training data; the network is similar to the unilateral extrapolation network, however it does not need to extrapolate as far beyond the training data. The unilateral extrapolation network achieves an RMSE of 0.161 after 5000 epochs. Figures 7.12 and 7.13 show the predicted and measured

maximum temperature and maximum temperature *difference*.

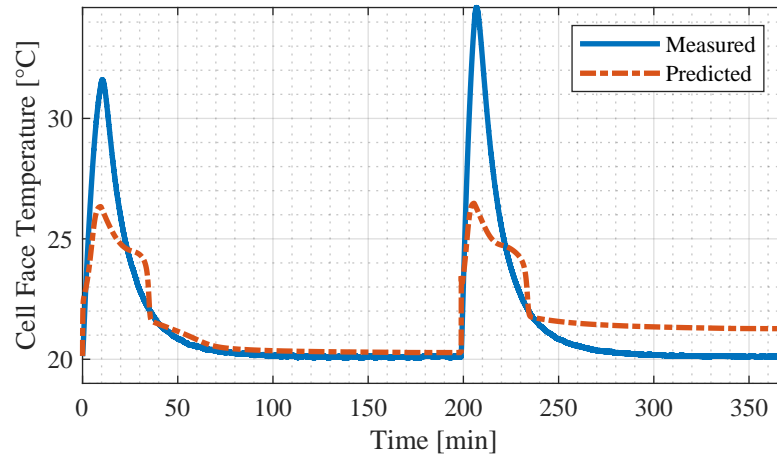


Figure 7.12: Unilateral extrapolation network predicted maximum cell temperature compared to measured values for 4C and 5C charges (validation set).

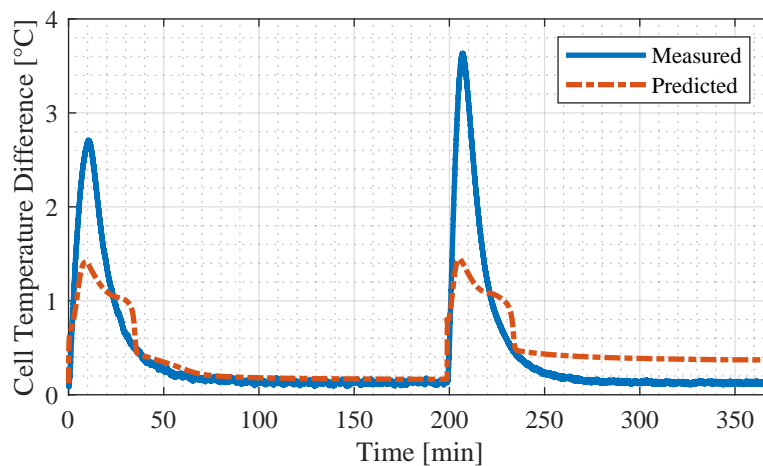


Figure 7.13: Unilateral extrapolation network predicted maximum cell temperature *difference* compared to measured values for 4C and 5C charges (validation set).

From these figures, it is clear that the network is unable to extrapolate effectively beyond the training set to higher C-rate charges. During the 4C and 5C charges, the

network under-predicts the maximum temperature by 5.3 °C and 8.1 °C, respectively; this is equivalent to over-predicting the temperature *rise* by 45% and 56%.

The maximum temperature profile predicted for the 4C and 5C charges by this network are nearly identical, which indicates that the neural network is unable to effectively learn the non-linear effect of charging current on cell temperatures. This symptom may be indicative of the lack of sufficient training data, and may be exacerbated by the extent to which the network must extrapolate beyond the training data.

It should also be noted that there is a significant difference between the 5C charge temperatures predicted by this network and by the bilateral extrapolation network. This provides further evidence that extrapolating charging current beyond the training data set yields a significant decrease in modelling accuracy and should be avoided.

Comparison of Network Performance

Since the networks are predicting temperatures for different current magnitudes, comparison must be drawn on a relative scale. Calculating the percentage error in maximum temperature requires a datum. A datum of 0 °C or absolute zero would be arbitrary in this context; the logical datum would be 20 °C (the datum used to calculate temperature rise), since this is the initial temperature of the battery module and the temperature of the cooling fluid and surrounding air. A datum of 20 °C, however, would cause very large, skewed values of relative error before and after each charge, where the temperatures remain near 20 °C. To eliminate the dependence

on a datum, the percentage error in maximum temperature *difference* across the cell face is used to compare performance of the three networks. The drawback to this approach is that error may appear larger following the cooling-off period, when the maximum temperature difference has been alleviated and the denominator of the relative error becomes very small.

The percentage error in maximum temperature *difference* is shown in Figure 7.14. It should be noted that a large amount of error is observed upon initialization, due to the fact that LSTM networks require feedback for initialization. Since this feedback is unavailable in the first time step, the network must make an assumption resulting in a relatively large initialization error. This error is quickly corrected in the proceeding time steps. These initialization errors are disregarded in the interpretation.

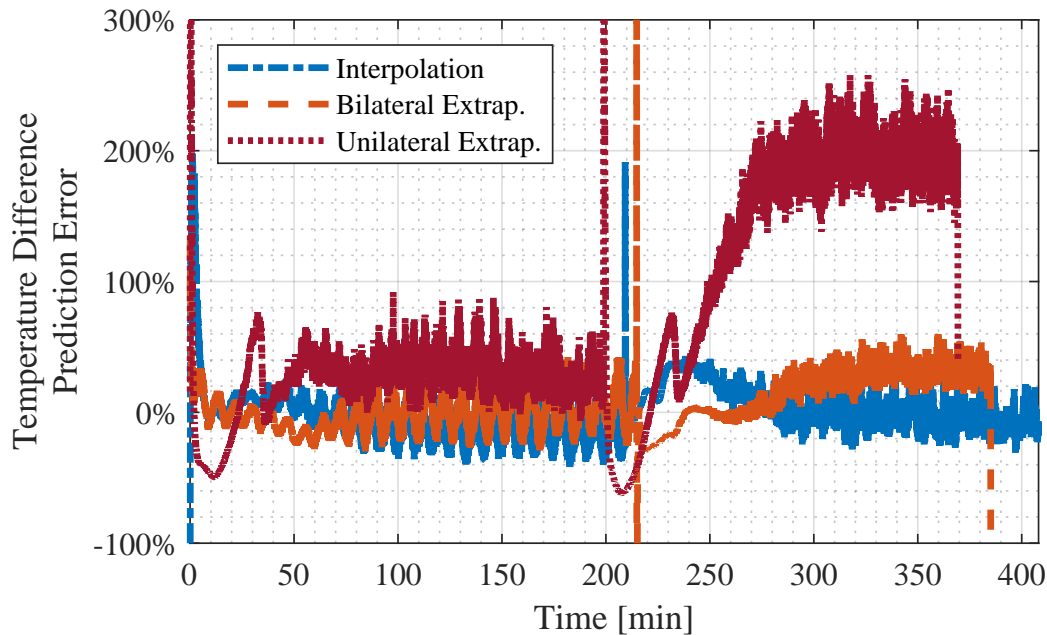


Figure 7.14: Percentage error of predicted maximum cell temperature *difference* as compared to experimental data (for respective validation sets).

Unsurprisingly, the neural network performs best when interpolating the outputs. The farther the network must extrapolate beyond the training data, the greater the error. This is immediately apparent in Figure 7.14. The relative error in the prediction of maximum temperature by the interpolative network is largely within 20%, with the greater errors corresponding to the periods where there is a high rate of change in the internal heat generation. The bilateral extrapolation network yields noticeably decreased performance, with error reaching 50% and settling at a higher level than the interpolative network. Prediction error from the unilateral extrapolation network is significantly greater: over 60% during constant current charging and settling far above the measured value. The RMSE for each network is summarized in Table 7.2.

Table 7.2: Validation RMSE of the different networks.

Test Case	Interpolation	Bilateral Extrapolation	Unilateral Extrapolation
RMSE	3.8%	5.4%	16.1%

Despite the networks having no underlying physical knowledge of the cell or module (or any part of the system) being modelled, an RMSE of 3.8% is achieved using the interpolative network. By including a 4C charge in the training set, the bilateral extrapolation network was able to reduce the RMSE from 16.1% to 5.4%, despite being trained on the same amount of data. This demonstrates the importance of a diverse training data set, spanning the full range of inputs that would be encountered in application.

In application, a neural network to be deployed on-board an EV—to be used for online temperature estimation or augmentation of measured pack temperature

distribution—would be trained on a wide range of data, extending *beyond* the allowable operating range, to avoid extrapolation. This is easily achieved since the battery of an EV should not operate at electrical current levels beyond what has been tested in a laboratory setting and deemed safe.

7.2.3 Comparison of Modelling Methods

The interpolative network is used for comparison as it demonstrates the greatest accuracy and is no less feasible or costly to develop than any of the other networks. Figure 7.15 shows the measured cell face temperature during the 2C and 4C charges, along with the temperatures predicted by the RNN and the CFD model.

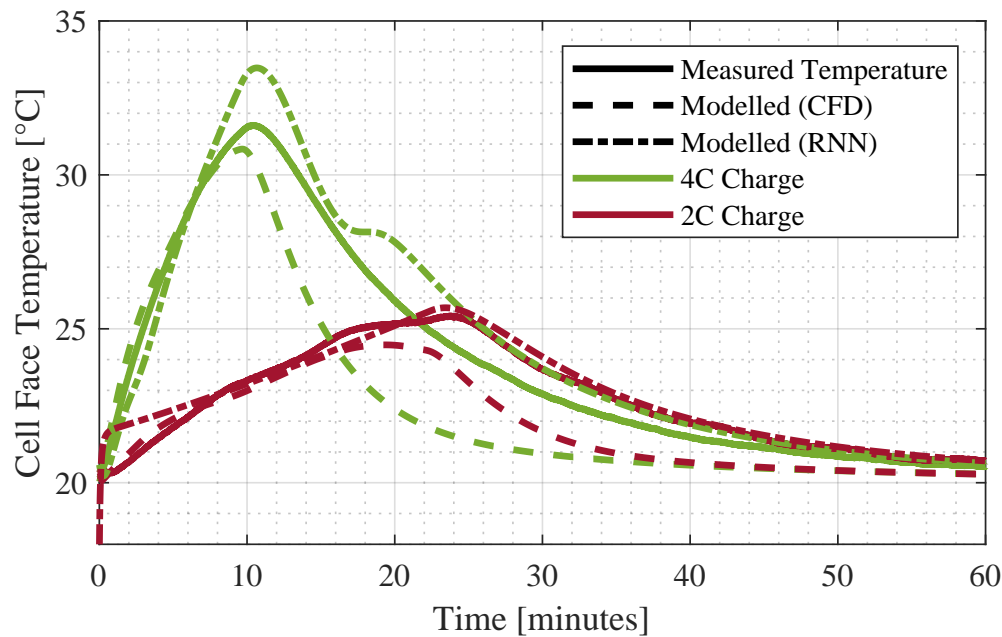


Figure 7.15: Measured and modelled cell surface temperature for 2C and 4C charges. Cell surface temperature corresponds to location TC3 for measured data and RNN predictions, and TC2 and TC3 for the CFD model, as indicated in 7.1a.

For the 4C charge shown in Figure 7.15, a peak temperature of 31.6 °C is measured; this is modelled as 30.8 °C using the CFD model, and predicted as 33.5 °C by the RNN. This figure also shows that the period following the constant-current portion of the charge (where the temperature begins to fall) is predicted more accurately using the RNN than the CFD model. This may be explained by the dependence of the CFD model on thermal properties of the battery cells, which are estimated using values for a similar cell, as discussed in Section 3.4.1. Since the CFD model employs symmetry planes to reduce the width and thickness of the cell (see Figure 6.3), it also does not entirely represent the spatial variations in temperature across the cell. The RNN, however, shows a point of inflection following the temperature peak. This point of inflection does not have a physical meaning and demonstrates the drawbacks of a model lacking physical understanding of the underlying system.

Chapter 8

Conclusion

This work explores many important considerations for designing fast-charging-capable battery modules and packs. Novel contributions are presented relating to the development and modelling of a fast-charging-capable battery module with consideration for the unique challenges thereof. This thesis also presents the development of a test procedure for characterization of the entropic heating coefficient, which involves additional experimental challenges.

Beginning with cell characterization ensures that a suitable cell is selected for implementation in a pack. Comparing cells based on effective energy density allows consideration for cooling system size, which has a dramatic effect on the energy density of a battery pack. For the four candidate cells, the characterization tests are used to determine charging efficiency, SOC at transition from constant-current to constant-voltage charging, equivalent resistance, time to add 80% SOC, and peak loss for a series of increasing charge rates. For the A123 NMC cell, increasing the constant

current charge rate from 4C to 5C yielded no decrease in time required to add 80% SOC since the charging voltage limit is reached at a much lower SOC, prompting the switch to constant voltage charging much earlier; furthermore the increased charge rate caused the peak loss to increase by 60%, illustrating the importance of cell selection for fast charging applications.

Once characterized, simplified thermal models are built for each of the four cells. From these models, an inter-cell cooling plate is sized for each cell such that the temperature rise during fast charging is maintained to within an acceptable level. Once the inter-cell cooling plate is sized, an effective energy density is calculated for each case, taking into account the cooling requirements of the cell and facilitating more effective comparison between cells. For the A123 NMC cell, increasing the inter-cell cooling plate thickness from 10% to 25% of cell thickness yields a 16% decrease in effective energy density. From this study, it is also determined that two-sided cooling, as opposed to one-sided cooling, is required to maintain reasonable peak temperature and temperature gradient.

For a selected cell, an actively cooled, 3p1s, test module is designed and constructed. The test module is intended to mimic the simplified model, utilizing two cold plates, one at either side of the cells, through which coolant is circulated.

A test plan is then developed and carried out for the test module. An entropic heating coefficient map is obtained through characterization and used in a cell loss model to predict heat generation in the cells at charge rates from 1C to 5C. The entropic heating coefficient shows no significant temperature dependence within the

range of temperatures tested. Using the developed heat generation model, the reversible heat is found to contribute up to 26% as much heat as the irreversible losses in the exothermic region, and up to 62% as much heat as the irreversible losses in the endothermic region. The ratio of reversible heat to irreversible heat decreases significantly as the charge rate is increased. Even for a 5C charge, however, the maximum exothermic reversible heat generation reaches approximately 10% of the maximum irreversible heat generation in the cell, showing that the reversible losses should be considered even at higher charge rates. For a 4C charge, it is also found that charging efficiency, based on modelled peak cell loss, increases from 91% to 93% when the temperature of the coolant increases from 15 °C to 25 °C—corresponding to a savings of more than 7 kW at fast charge rates, which would then be compounded by reduced thermal management loads.

For the battery module, detailed fluid flow and thermal models are developed using CFD in ANSYS Fluent and ANSYS Mechanical. For a series of increasing-rate charges up to 5C, and cycle composed of repeated driving and 4C charging, module temperatures obtained through laboratory testing are compared to those obtained using the numerical models. In addition to the physics-based modelling, three different recurrent neural networks are trained on the experimental data to predict the maximum temperature and maximum temperature *difference* across the cell under the 1C to 5C charge rates. The first network is trained to interpolate the temperature outputs, the second is trained to extrapolate under higher charge rates, and third is trained to extrapolate temperature outputs for both higher and lower charge rates. The interpolative network shows superior performance, with a validation RMSE of

3.8%, compared to 5.4% and 16.1% for the bilateral and unilateral extrapolations networks, respectively. The predictions made by the recurrent neural networks are compared with the CFD modelling and the experimental data obtained from test module. For a 4C charge, a peak temperature of 31.6 °C is measured in the laboratory, modelled using CFD as 30.8 °C, and predicted by the recurrent neural network as 33.5 °C.

8.1 Future Work

The study of temperature impact on ageing at varying charge rates presented in Section 2.1.3 and the cell loss and efficiency trends presented in Section 5.5.2 show potential for the development of improved charging procedures for higher charge rates. These results show that it may be possible to reduce charging losses and thermal management system requirements, while simultaneously increasing cycle life of the cells. The greater charging efficiency which may be achieved by operating closer to the upper temperature limit of the cells requires an effective thermal management system which maintains a uniform temperature across the cell and pack. This gives rise to a trade-off between thermal management system mass and charging efficiency of the battery pack, which is reminiscent of the trade-off between energy density and power density of the battery cell. Increased temperature uniformity also ensures that the thermal capacitance of the battery pack can be leveraged as much as possible to aid in fast charging. Future work should include a study of thermal management

system mass versus charging efficiency. The work presented in this thesis, particularly in Section 5.5.2, shows that effective thermal management of the battery pack is not simply a problem of cooling the cells as much as is feasible, and that thermal loads may be reduced by considering the temperature of the cells. A thermal management system which is better able to maintain temperature uniformity in the battery cells may achieve higher charging efficiency by taking advantage of lower internal resistances at increased temperatures.

In order to improve the accuracy of the numerical temperature modelling, it is recommended to expand the model to include the cell tabs, to model current density and spatially-varying heat generation in the cells (preventing the use of symmetry planes), and to further investigate the thermal properties of the battery cells. As it is not represented in the model, or necessarily representative or desirable, it may also be useful to isolate heat loss through cyclers leads by bringing them to thermal equilibrium with the cell tabs. The cooling capacity of the chiller is not expected to contribute to the discrepancy between measured and modelled temperatures during fast charging. This is evidenced by the lack of significant temperature rise of the coolant at the inlet of the cold plate. It is recommended that any future work begin by addressing the model refinements discussed here and re-assessing any discrepancies that may remain.

The results of the thermal modelling using neural networks shows promise and warrants further investigation. Different types of neural networks may be investigated and the model may be scaled to pack-level. This could be used on-board an EV for enhancing the resolution of the measured temperature distribution within the

battery pack, while minimizing the number of physical sensors embedded. Future work in this area should include acquisition of more training data—including charging and discharging at different rates and a variety of drive cycles—to improve the diversity of the training data and the applicability of the model. Modelled cell temperature resolution may also be enhanced in future work, depending on the training data available.

Validation of the entropic heating coefficient and heat generation model requires an isothermal calorimeter. For this reason, it may be more practical to characterize a cylindrical battery cell, which is better suited for commercially available calorimeters. This test would provide validation for the transient heat generation predicted by the model.

References

- [1] B. Bilgin, P. Magne, P. Malysz, Y. Yang, V. Pantelic, M. Preindl, A. Korobkine, W. Jiang, M. Lawford, A. Emadi, Making the case for electrified transportation, *IEEE Transactions on Transportation Electrification* 1 (1) (2015) 4–17.
- [2] L. Lu, X. Han, J. Li, J. Hua, M. Ouyang, A review on the key issues for lithium-ion battery management in electric vehicles, *Journal of power sources* 226 (2013) 272–288.
- [3] A. M. Andwari, A. Pesiridis, S. Rajoo, R. Martinez-Botas, V. Esfahanian, A review of battery electric vehicle technology and readiness levels, *Renewable and Sustainable Energy Reviews* 78 (2017) 414–430.
- [4] Tesla model 3 battery pack & battery cell teardown highlights performance improvements — cleantechnica, <https://cleantechnica.com/2019/01/28/tesla-model-3-battery-pack-cell-teardown-highlights-performance-improvements/>, (Accessed on 05/17/2020).
- [5] G. Girishkumar, B. McCloskey, A. C. Luntz, S. Swanson, W. Wilcke, Lithium-air battery: promise and challenges, *The Journal of Physical Chemistry Letters*

- 1 (14) (2010) 2193–2203.
- [6] Electric vehicles — mobility and transport, https://ec.europa.eu/transport/themes/urban/vehicles/road/electric_en, (Accessed on 05/17/2020).
- [7] A. Tomaszewska, Z. Chu, X. Feng, S. O’Kane, X. Liu, J. Chen, C. Ji, E. Endler, R. Li, L. Liu, et al., Lithium-ion battery fast charging: a review, *ETransportation* 1 (2019) 100011.
- [8] Porsche is bringing its ultra-fast electric car charging stations to the us - electrek, <https://electrek.co/2017/09/19/porsche-ultra-fast-charging-stations-electric-cars-us/>, (Accessed on 05/18/2020).
- [9] U. S. Kim, J. Yi, C. B. Shin, T. Han, S. Park, Modelling the thermal behaviour of a lithium-ion battery during charge, *Journal of Power Sources* 196 (11) (2011) 5115–5121.
- [10] S. Al Hallaj, H. Maleki, J.-S. Hong, J. R. Selman, Thermal modeling and design considerations of lithium-ion batteries, *Journal of power sources* 83 (1-2) (1999) 1–8.
- [11] K. Onda, T. Ohshima, M. Nakayama, K. Fukuda, T. Araki, Thermal behavior of small lithium-ion battery during rapid charge and discharge cycles, *Journal of Power sources* 158 (1) (2006) 535–542.
- [12] X.-G. Yang, C.-Y. Wang, Understanding the trilemma of fast charging, energy density and cycle life of lithium-ion batteries, *Journal of Power Sources* 402 (2018) 489–498.

- [13] Y. Xiao, Model-based virtual thermal sensors for lithium-ion battery in ev applications, *IEEE Transactions on Industrial Electronics* 62 (5) (2014) 3112–3122.
- [14] C. Mao, R. E. Ruther, J. Li, Z. Du, I. Belharouak, Identifying the limiting electrode in lithium ion batteries for extreme fast charging, *Electrochemistry Communications* 97 (2018) 37–41.
- [15] Y. Tang, Y. Zhang, W. Li, B. Ma, X. Chen, Rational material design for ultrafast rechargeable lithium-ion batteries, *Chemical Society Reviews* 44 (17) (2015) 5926–5940.
- [16] L. H. Saw, Y. Ye, A. A. Tay, Integration issues of lithium-ion battery into electric vehicles battery pack, *Journal of Cleaner Production* 113 (2016) 1032–1045.
- [17] R. J. Brodd, *Batteries for sustainability: selected entries from the encyclopedia of sustainability science and technology*, Springer Science & Business Media, 2012.
- [18] M. H. Lipu, M. Hannan, A. Hussain, M. Hoque, P. J. Ker, M. Saad, A. Ayob, A review of state of health and remaining useful life estimation methods for lithium-ion battery in electric vehicles: Challenges and recommendations, *Journal of cleaner production* 205 (2018) 115–133.
- [19] Y. Li, X. Feng, D. Ren, M. Ouyang, L. Lu, Varying thermal runaway mechanism caused by fast charging for high energy pouch batteries, in: *ECS Meeting Abstracts MA2019-01*, Vol. 6, 2019, p. 585.

- [20] T. Waldmann, M. Wilka, M. Kasper, M. Fleischhammer, M. Wohlfahrt-Mehrens, Temperature dependent ageing mechanisms in lithium-ion batteries—a post-mortem study, *Journal of Power Sources* 262 (2014) 129–135.
- [21] S. Zhang, K. Xu, T. Jow, The low temperature performance of li-ion batteries, *Journal of Power Sources* 115 (1) (2003) 137–140.
- [22] J. Lempert, P. Kollmeyer, P. Malysz, O. Gross, J. Cotton, A. Emadi, Battery entropic heating coefficient testing and use in cell-level loss modeling for extreme fast charging, *SAE International Journal of Advances and Current Practices in Mobility* (2020).
- [23] Evolving economics of electric vehicle batteries: Part 1 — vaneck, <https://www.vaneck.com/ucits/blog/natural-resources/the-evolution-of-electric-vehicle-batteries-part-1/de>.
- [24] Johnson Matthey Battery Systems, Our guide to batteries, 3rd edition, <http://www.jmbatterysystems.com/technology/our-guide-to-batteries> (2017).
- [25] Y. Ye, L. H. Saw, Y. Shi, K. Somasundaram, A. A. Tay, Effect of thermal contact resistances on fast charging of large format lithium ion batteries, *Electrochimica Acta* 134 (2014) 327–337.
- [26] The Tesla Team, Introducing v3 supercharging — tesla canada, https://www.tesla.com/en_CA/blog/introducing-v3-supercharging (March 2019).

- [27] M. Kane, Porsche opens europe's most powerful fast-charging park, <https://insideevs.com/news/400051/porsche-europe-most-powerful-fast-charging-park/> (February 2020).
- [28] Locate a public ev charger — electrify america, <https://www.electrifyamerica.com/locate-charger/> (July 2020).
- [29] S. Bazinski, X. Wang, The influence of cell temperature on the entropic coefficient of a lithium iron phosphate (lfp) pouch cell, *Journal of The Electrochemical Society* 161 (1) (2014) A168–A175.
- [30] J. Zhang, J. Huang, Z. Li, B. Wu, Z. Nie, Y. Sun, F. An, N. Wu, Comparison and validation of methods for estimating heat generation rate of large-format lithium-ion batteries, *Journal of Thermal Analysis and Calorimetry* 117 (1) (2014) 447–461.
- [31] D. Bernardi, E. Pawlikowski, J. Newman, A general energy balance for battery systems, *Journal of the electrochemical society* 132 (1) (1985) 5–12.
- [32] J.-S. Hong, H. Maleki, S. Al Hallaj, L. Redey, J. Selman, Electrochemical-calorimetric studies of lithium-ion cells, *Journal of the Electrochemical Society* 145 (5) (1998) 1489–1501.
- [33] V. V. Viswanathan, D. Choi, D. Wang, W. Xu, S. Towne, R. E. Williford, J.-G. Zhang, J. Liu, Z. Yang, Effect of entropy change of lithium intercalation in cathodes and anodes on li-ion battery thermal management, *Journal of Power Sources* 195 (11) (2010) 3720–3729.

- [34] Q. Wang, B. Jiang, B. Li, Y. Yan, A critical review of thermal management models and solutions of lithium-ion batteries for the development of pure electric vehicles, *Renewable and Sustainable Energy Reviews* 64 (2016) 106–128.
- [35] R. E. Williford, V. V. Viswanathan, J.-G. Zhang, Effects of entropy changes in anodes and cathodes on the thermal behavior of lithium ion batteries, *Journal of Power Sources* 189 (1) (2009) 101–107.
- [36] SAE International, J2344, guidelines for electric vehicle safety (2010).
- [37] C. Forgez, D. V. Do, G. Friedrich, M. Morcrette, C. Delacourt, Thermal modeling of a cylindrical lifepo₄/graphite lithium-ion battery, *Journal of Power Sources* 195 (9) (2010) 2961–2968.
- [38] S. Chacko, Y. M. Chung, Thermal modelling of li-ion polymer battery for electric vehicle drive cycles, *Journal of Power Sources* 213 (2012) 296–303.
- [39] Y. Huo, Z. Rao, X. Liu, J. Zhao, Investigation of power battery thermal management by using mini-channel cold plate, *Energy Conversion and Management* 89 (2015) 387–395.
- [40] A. Jarrett, I. Y. Kim, Design optimization of electric vehicle battery cooling plates for thermal performance, *Journal of Power Sources* 196 (23) (2011) 10359–10368.
- [41] T. Deng, G. Zhang, Y. Ran, Study on thermal management of rectangular li-ion battery with serpentine-channel cold plate, *International Journal of Heat and Mass Transfer* 125 (2018) 143–152.

- [42] S. Panchal, I. Dincer, M. Agelin-Chaab, R. Fraser, M. Fowler, Thermal modeling and validation of temperature distributions in a prismatic lithium-ion battery at different discharge rates and varying boundary conditions, *Applied Thermal Engineering* 96 (2016) 190–199.
- [43] K. Fang, D. Mu, S. Chen, B. Wu, F. Wu, A prediction model based on artificial neural network for surface temperature simulation of nickel–metal hydride battery during charging, *Journal of power sources* 208 (2012) 378–382.
- [44] M. Al-Zareer, I. Dincer, M. A. Rosen, A novel phase change based cooling system for prismatic lithium ion batteries, *International Journal of Refrigeration* 86 (2018) 203–217.
- [45] S. Panchal, K. Gudlanarva, M.-K. Tran, R. Fraser, M. Fowler, High reynold’s number turbulent model for micro-channel cold plate using reverse engineering approach for water-cooled battery in electric vehicles, *Energies* 13 (7) (2020) 1638.
- [46] P. T. Tennessen, J. C. Weintraub, W. A. Hermann, Extruded and ribbed thermal interface for use with a battery cooling system, uS Patent 8,758,924 (Jun. 24 2014).
- [47] C. Zhao, W. Cao, T. Dong, F. Jiang, Thermal behavior study of discharging/charging cylindrical lithium-ion battery module cooled by channeled liquid flow, *International journal of heat and mass transfer* 120 (2018) 751–762.

- [48] J. Sieg, J. Bandlow, T. Mitsch, D. Dragicevic, T. Materna, B. Spier, H. Witzenhäusen, M. Ecker, D. U. Sauer, Fast charging of an electric vehicle lithium-ion battery at the limit of the lithium deposition process, *Journal of Power Sources* 427 (2019) 260–270.
- [49] D. Anseán, M. González, J. Viera, V. García, C. Blanco, M. Valledor, Fast charging technique for high power lithium iron phosphate batteries: A cycle life analysis, *Journal of Power Sources* 239 (2013) 9–15.
- [50] N. Nieto, L. Díaz, J. Gastelurrutia, F. Blanco, J. C. Ramos, A. Rivas, Novel thermal management system design methodology for power lithium-ion battery, *Journal of Power Sources* 272 (2014) 291–302.
- [51] D. Tracy, An extremely detailed look at the porsche taycan’s engineering designed to take on tesla, <https://jalopnik.com/an-extremely-detailed-look-at-the-porsche-taycans-engin-1837802533> (September 2019).
- [52] F. Lambert, Porsche taycan to have 250 kw charging at launch, promised 350 kw coming in 2021 - electrek, <https://electrek.co/2019/07/17/porsche-taycan-250-kw-charging-launch-promised-350-kw/> (July 2019).
- [53] United states advanced battery consortium battery test manual for hybrid electric vehicles (Jun 2015).
URL https://www.uscar.org/commands/files_download.php?files_id=40

- [54] S.-L. Wu, W. Zhang, X. Song, A. K. Shukla, G. Liu, V. Battaglia, V. Srinivasan, High rate capability of li (ni_{1/3}mn_{1/3}co_{1/3}) o₂ electrode for li-ion batteries, *Journal of The Electrochemical Society* 159 (4) (2012) A438.
- [55] P. J. Kollmeyer, A. Shridar, T. Jahns, Modeling of low-temperature operation of a hybrid energy storage system with a butler-volmer equation based battery model, in: 2016 IEEE Energy Conversion Congress and Exposition (ECCE), IEEE, 2016, pp. 1–8.
- [56] S. M. Lukic, J. Cao, R. C. Bansal, F. Rodriguez, A. Emadi, Energy storage systems for automotive applications, *IEEE Transactions on industrial electronics* 55 (6) (2008) 2258–2267.
- [57] M. Yilmaz, P. T. Krein, Review of battery charger topologies, charging power levels, and infrastructure for plug-in electric and hybrid vehicles, *IEEE transactions on Power Electronics* 28 (5) (2012) 2151–2169.
- [58] W. Song, M. Chen, F. Bai, S. Lin, Y. Chen, Z. Feng, Non-uniform effect on the thermal/aging performance of lithium-ion pouch battery, *Applied thermal engineering* 128 (2018) 1165–1174.
- [59] M. Fleckenstein, O. Bohlen, M. A. Roscher, B. Bäker, Current density and state of charge inhomogeneities in li-ion battery cells with lifepo₄ as cathode material due to temperature gradients, *Journal of Power Sources* 196 (10) (2011) 4769–4778.

- [60] Table 8-3-1 – properties of mixture water/glycol, <https://detector-cooling.web.cern.ch/data/Table%208-3-1.htm>, (Accessed on 04/22/2020).
- [61] I. Wakefield-Vette, 180-10,180-11.pdf, <http://www.wakefield-vette.com/Portals/0/resources/datasheets/180-10,180-11.pdf>, (Accessed on 05/14/2020).
- [62] Y. Ye, L. H. Saw, Y. Shi, K. Somasundaram, A. A. Tay, Effect of thermal contact resistances on fast charging of large format lithium ion batteries, *Electrochimica Acta* 134 (2014) 327–337.
- [63] J. Yi, U. S. Kim, C. B. Shin, T. Han, S. Park, Three-dimensional thermal modeling of a lithium-ion battery considering the combined effects of the electrical and thermal contact resistances between current collecting tab and lead wire, *Journal of the Electrochemical Society* 160 (3) (2013) A437–A443.
- [64] K. E. Thomas, C. Bogatu, J. Newman, Measurement of the entropy of reaction as a function of state of charge in doped and undoped lithium manganese oxide, *Journal of the Electrochemical Society* 148 (6) (2001) A570–A575.
- [65] P. Kollmeyer, A. Hackl, A. Emadi, Li-ion battery model performance for automotive drive cycles with current pulse and eis parameterization, in: 2017 IEEE Transportation Electrification Conference and Expo (ITEC), IEEE, 2017, pp. 486–492.
- [66] F. R. Menter, Two-equation eddy-viscosity turbulence models for engineering applications, *AIAA journal* 32 (8) (1994) 1598–1605.

- [67] V. Gnielinski, New equations for heat and mass transfer in turbulent pipe and channel flow, *Int. Chem. Eng.* 16 (2) (1976) 359–368.
- [68] S. Hochreiter, J. Schmidhuber, Long short-term memory, *Neural computation* 9 (8) (1997) 1735–1780.
- [69] The MathWorks Inc., Long short-term memory networks.
URL <https://www.mathworks.com/help/deeplearning/ug/long-short-term-memory-networks.html>